An Experimental Investigation of Roll and Yaw Coupled Oscillations of a Delta Wing

by

John Forrest Clay Walker

A thesis submitted to the Graduate Faculty of
Auburn University
in partial fulfillment of the
requirements for the Degree of
Master of Science

Auburn, Alabama
May 9, 2011

Approved by

Anwar Ahmed, Chair, Professor of Aerospace Engineering
Gilbert Crouse, Associate Professor of Aerospace Engineering
Roy Hartfield, Professor of Aerospace Engineering

Abstract

An experimental investigation was undertaken to study roll and yaw coupled oscillation of a delta wing. Results indicated that the oscillations started at a mean α = 29 for all cases. Beyond which the amplitude of oscillations amplified indicating that the axial stability of the vortex propagates upstream at which point the wing oscillations peak. The existence of an onset of oscillation angle was found. Consequently, a self sustaining limit cycle was observed for roll - free, yaw - free and the all - free test case. A sinusoidal oscillation in C_L was observed for all cases as well as a linear increase in mean C_L with increasing angle of attack. The coupling effect of roll and yaw exhibited an attenuation of the amplitude of roll and yaw oscillation. Canard and double delta wing configurations were tested as passive flow control devices to dampen wing roll and side slip. These configurations not only effectively decreased both roll and yaw oscillations, a large increase in the C_L was also observed. For both the canard and the double delta wing configurations the wing roll oscillation decreased

significantly and side slip disappeared all together. A delay in stall and an increase in C_D were also noted.

Acknowledgments

The author would like to thank Dr. Anwar Ahmed for his guidance and support throughout the course of this effort. Thanks are also due to Mr. Hamza Ahmed and Mr. Hayden Moore for their help in setting up experiments and anything else that might have assisted in, large or small. Many thanks go to Andy Weldon for the advice and work he put into every piece machined for this project. The author would also like to thank his father, Ray Walker, for his efforts to motivate me and keep me level headed. For that and many other things far too numerous to mention, thanks.

Table of Contents

Abstract ii

Acknowledgments iv

Nomenclature viii

List of Figures x

List of Tables xv

Introduction 1

1.1 Types of Delta Wing 2

1.2 Vortex Lift 3

1.3 Vortex Bursting 4

1.3.1 Bubble Type Bursting 5

1.3.2 Spiral Type Bursting 6

1.3.3 Significance of Vortex Bursting 6

1.4 Previous Research 7

1.5 Vortex Breakdown Theories 10

1.5.1 Core Stagnation 11

1.5.2 Ludwieg's Spiral Instability Theory 11
1.6 Flight Dynamic Phenomena 12
1.6.1 Wing Rock 12
1.6.2 Wing Drop 12
1.6.3 Nose Slice 13
1.7 Vortex Flow Control Methods 13
1.7.1 Blowing and Suction 14
1.7.2 Unsteady Excitation 15
1.8 Research Motivation 15
Experimental Setup 17
2.1 Test Facilities 17
2.2 Model Description 17
2.2.1 Model Mounting 18
2.3 Passive Flow Control Methods 19
2.3.1 Canard 19
2.3.2 Double Delta Wing 19
2.4 Instrumentation 20
2.4.1 Roll Measurements 20
2.4.2 Yaw Measurements 20
2.5 Wind Tunnel Flow Visualization 21

Results and Discussion 22

3.1 Fixed Wing Case 22

3.2 Roll - Free Case 23

3.2 Yaw - Free Case 25

3.4 All - Free Case 27

3.5 Canard Attachment 30

3.6 Double Delta Attachment 31

3.7 Canard and Double Delta Attachment 31

Conclusions 32

Recommendation 36

References 37

Figures 42

Appendix B 80

List of Tables 80

Appendix C 82

Additional Plots 82

Appendix D 89

Uncertainty Analysis 89

Nomenclature

A	=	Planform Area
c	=	Root Chord
C_D	=	Coefficient of Drag $(\frac{D}{qA})$
C_L	=	Coefficient of Lift $(\frac{L}{qA})$
C_{RM}	=	Coefficient of Rolling Moment $(\frac{RM}{qAc})$
C_{SF}	=	Coefficient of Side Force $(\frac{SF}{qA})$
C_{YM}	=	Coefficient of Yawing Moment $(\frac{YM}{qAc})$
L	=	Lift
q	=	Dynamic Pressure $(\frac{\rho V^2}{2})$
r	=	Radius
Re	=	Reynolds Number $(\frac{\rho Vc}{\mu})$
V_∞	=	Free Stream Velocity
x	=	Axial Distance

α = Angle of Attack

β = Yaw Angle

Γ = Circulation

Λ = Wing Leading Edge Sweep Angle

ϱ = Density

ϕ = Roll Angle

List of Figures

Figure 1: Coefficient of lift versus angle of attack for a classical delta wing [41] . 42

Figure 2: Mig 21 [42] 43

Figure 3: Convair F-102A [43] 43

Figure 4: B-58 Hustler [44] 43

Figure 5: Primary versions of the delta wing platform [45]..... 44

Figure 6: Detachment of flow along the leading edge [13] 44

Figure 7: Topology of flow over a delta wing [1]..... 45

Figure 8: Spiral and bubble type bursting [46] 45

Figure 9: Bubble Type Bursting [13]..... 46

Figure 10: Spiral Type Bursting [13]..... 46

Figure 11: Asymmetric vortex position [47]..... 47

Figure 12: Delta wing model 48

Figure 13: Delta wing model 48

Figure 14: Mounting System 49

Figure 15: Canard configuration on delta wing 49

Figure 16: Double delta wing configuration on delta wing 50

Figure 17: Us Digital HB6M Optical Encoder [48] 50

Figure 18: Optical Encoder [48] 51

Figure 19: Honeywell HC1512 sensor schematic diagram [49] 51

Figure 20: Honeywell HC1512 sensor circuit board [49] 52

Figure 21: Honeywell HC1512 sensor [49] 52

Figure 22: HC1512 sensor placement 52

Figure 23: Time history of Lift and AoA – fixed wing case 53

Figure 24: Time history of Lift and AoA expanded – fixed wing case 53

Figure 25: Time history of Drag and AoA – fixed wing case 54

Figure 26: Time history of Drag and AoA expanded – fixed wing case 54

Figure 27: Fixed wing case flow visualization 55

Figure 28: Time history of Lift and wing roll – roll - free case 56

Figure 29: Phase Portrait of Roll – roll - free case 56

Figure 30: Extended Phase Portrait – roll - free case 57

Figure 31: Time history of Side Force and wing roll – roll - free case 57

Figure 32: Time history of Rolling Moment and wing roll – roll - free case 58

Figure 33: Time history of wing roll – roll - free case 58

Figure 34: Roll and AoA vs. Time expanded –roll - free case 58

Figure 35: Time history of Lift and wing roll – roll - free case 59

Figure 36: Roll - free case flow visualization 60

Figure 37: Time history of Lift and side slip – yaw - free case 61

Figure 38: Phase Portrait of Yaw – yaw - free case..... 61

Figure 39: Extended Phase Portrait – yaw - free case 62

Figure 40: Time history of Side Force and side slip – yaw - free case 62

Figure 41: Time history of side slip – yaw - free case 63

Figure 42: Time history of side slip expanded – yaw - free case..... 63

Figure 43: Time history of Lift expanded – yaw - free case 63

Figure 44: Time history of Drag - yaw - free case..... 64

Figure 45: yaw - free case flow visualization 65

Figure 46: The Coefficient of Lift vs. AoA 66

Figure 47: Drag Polar..... 66

Figure 48: Time history of Lift, wing roll and side slip - all - free case 67

Figure 49: Yaw vs. Roll (All - free)..... 67

Figure 50: Phase Portrait of Roll – all - free case..... 68

Figure 51: Extended Phase Portrait of Roll – all - free case..... 68

Figure 52: Phase Portrait of Yaw – all - free case..... 69

Figure 53: Extended Phase Portrait of Yaw – all - free case 69

Figure 54: Time history of Rolling Moment, wing roll and side slip - all - free case

..... 70

Figure 55: Time history of Yawing Moment, wing roll and side slip - all - free case 70

Figure 56: Time history of wing roll and side slip – all - free case 70

Figure 57: Time history of Lift - all - free case 71

Figure 58: Time history of Drag - all - free case 71

Figure 59: All - free case flow visualization 72

Figure 60: Time history of Lift – canard attachment 73

Figure 61: Time history of Drag – canard attachment 73

Figure 62: Time history of Lift and wing rock – canard attachment 73

Figure 63: Canard attachment flow visualization 74

Figure 64: Time history of Lift – Double Delta attachment 75

Figure 65: Time history of Drag – Double Delta attachment 75

Figure 66: Time history of Lift and wing rock – Double Delta attachment 75

Figure 67: Double Delta attachment flow visualization 76

Figure 68: Time history of Lift – Canard and Double Delta attachment 77

Figure 69: Time history of Drag – Canard and Double Delta attachment 77

Figure 70: Canard and Double Delta Attachment flow visualization 78

Figure 71: The Coefficient of Lift vs. AoA – passive flow control 79

Figure 72: C_{YM} and AoA vs. Time - fixed wing 82

Figure 73: Roll Coordinate System 83

Figure 74: Roll and C_{RM} vs. Time (b) – Roll - free 83

Figure 75: Roll and C_{SF} vs. Time (b) - roll - free 84

Figure 76: Yaw Coordinate System 85

Figure 77: Yaw and C_L vs. Time (b) - yaw - free 85

Figure 78: Yaw and C_{RM} vs. Time (b) - yaw - free 86

Figure 79: Yaw and C_{SF} vs. Time (b) – yaw - free 86

Figure 80: Roll, Yaw and C_{RM} vs. Time (b) - all - free 87

Figure 81: Roll, Yaw and C_{YM} vs. Time (b) - all - free 87

Figure 82: All Cases Phase Portraits 88

List of Tables

Table 1: Reduction Matrix 80

Table 2: Optical Encoder Parameters [48] 80

Table 3: Honeywell HC1512 sensor parameters [49] 81

Chapter 1

Introduction

The delta wing is a special case of a swept winged aircraft with a triangular planform closely resembling the Greek letter Δ [1]. Delta wings commonly have relatively short aspect ratios, large wing root chord and in many cases, a smaller leading edge radius.

Delta wings are used in many modern military fighter aircraft due to the favorable aerodynamic characteristics such as stall margins, maneuverability and low speed handling. Additionally, the delta wing design allows for a high critical Mach number due to the wing sweep and moderate wing thickness distribution. Furthermore, in supersonic flow the wing's leading edge remains behind the shockwave generated at the nose. Since the delta wing's root chord is large it offers more structural strength than the cantilevered swept wing.

The mechanism of delta wing lift generation consists of a combination of potential lift and lift due to vortices. But, by definition, a delta wing is a low aspect ratio wing which has a performance penalty of increased induced drag.

This results in a decrease in the lift to drag ratio in comparison to regular wings. At lower speeds a delta wing must pitch up to a higher angle of attack to maintain high lift that drastically increases the drag [2]. A typical coefficient of lift versus angle of attack for the classical delta wing can be seen in Figure 1.

1.1 Types of Delta Wing

There are several air vehicle platforms based on different delta wing configurations. The simplest delta wing is of the triangular shape and has a constant wing leading edge sweep. These wings are primarily used for high speed, high altitude interceptors, for example the Mig 21(Figure 2), Convair F-102A (Figure 3) or the B-58 Hustler (Figure 4). But many modern military aircraft use hybrid combinations of the delta wing to take advantage of the delta wing's favorable aerodynamic characteristics. There are four primary versions of the delta wing platform (Figure 5):

1.) Simple delta wing. This is commonly considered the pure delta wing and is characterized by a constant sweep. A slender – delta wing is a special category of the pure delta wing and is defined by any lifting platform with a sweep larger than 75 degrees.

2.) Cropped delta wing. The cropped delta is a classical delta wing with its wing tips cut off. This helps avoid tip drag at high angles of attack.

3.) Notched delta wing. The notched delta wing configuration has a similar design to the simple or pure delta wing, except there is a notch in the trailing edge that reduces wing area.

4.) Compound delta or double delta wing. This is characterized by an inner section with a larger wing sweep that eventually at a point along the leading edge, reduces the leading edge sweep. Compound delta configurations improve lift at high angles of attack and helps delay stall.

It should be noted that there is a version of the delta wing called the ogival delta wing. This configuration has a smoothly blended double curve that follows the leading edge and tip of a cropped delta wing. This configuration is not considered one of the basic delta wing configurations.

1.2 Vortex Lift

The flow over a delta wing is dominated by two counter rotating vortices that originate at the leading edge due to pressure difference between the upper and lower. Inviscid flow theory predicts an infinite velocity at a sharp convex corner. However, separation occurs due to the small radius of the leading edge (Figure 6). This detachment of the flow along the leading edge causes the flow to curl around the leading edge into a pair of strong counter-rotating vortices. The pressure difference between the upper and lower surfaces of the delta wing

become greater as the vortices become stronger with increasing angle of attack, leading to the unique mechanism of lift production compared to a flat plate [3](Figure 7). High values of lift coefficient C_L, critical Mach number, lift to drag ratio and high maneuverability are all due to the delta wing's unique lift-producing mechanism [4].

1.3 Vortex Bursting

With increasing angles of attack the vortices formed near the leading edge cannot maintain their tight structure and are susceptible to axial instability and breakdown over time. This breakdown occurs in the form of a rapid growth in the vortex diameter and a decrease in the axial velocity over a very short distance (Figure 8). This decrease in the axial velocity may lead to the formation of a stagnation point at the vortex burst location [5]. With increasing angle of attack vortex production outgrows convection and leads to asymmetric shedding of the vortices in the flow [6]

Leibovich [7] categorized the vortex flow field into three spatial regions:

1.) Approach flow field: This region mainly consists of a concentrated vortex core. Any changes in the flow of the axial distances are slow and predictable.

2.) Breakdown region: This regime is characterized by rapid changes in axial direction occupying axial intervals on the order of 5 vortex core diameters. The generation of a stagnation point is seen and the flow is the marked by a large increase in turbulent intensity.

3.) New vortex structure: A new vortex is formed with an expanding core is established downstream of the breakdown region.

Faler and Leibovich [8] made extensive studies including flow visualization and quantitative measurements to observe seven distinct structures numbering from 0 to 6. These structures included the two dominate forms of vortex bursting seen in the delta wing vortex breakdown phenomenon. Spiral and bubble bursting, are described below.

1.3.1 Bubble Type Bursting

Bubble type bursting, or B-type bursting, is characterized by a sudden expansion in the radial size of the vortex core and a sudden decrease in the core axial velocity over a short distance with evidence of a stagnation point on the swirl axis. Generally the swell or bubble is open downstream with an indication that the internal flow velocities are very low. Bornstein and Escudier, using laser-Doppler anemometer measurements, calculated axial velocity distributions

showed that near stagnation conditions exist in the interior of a vortex undergoing a B-type burst [9]. The Bubble type bursting is described in Figure 9

1.3.2 Spiral Type Bursting

Spiral type bursting is the most common form observed on a delta wing with a unique feature of the vortex core transitioning into an expanding spiral whose sign of rotation is opposite to the sign of vorticity. The vortex core normally takes the form of a spiral which continues for one to two turns before breaking up into large scale turbulence. Faler and Leibovich [8] found that for the spiral type bursting the frequency of rotation would increase and the spiral burst would change the forms to a bubble burst type. The burst location then moves rapidly upstream. This B-type bursting mode is only present for a few seconds and then changes abruptly back to a spiral mode while moving back downstream [8]. The spiral type bursting can be seen in Figure 10.

1.3.3 Significance of Vortex Bursting

The vortices created by the detachment of the flow along the leading edge are susceptible to axial instability and break down over time. This breakdown occurs in the form of a rapid growth in the vortex diameter and a decrease in the axial velocity over a short distance. This decrease in the axial velocity leads to the

formation of a stagnation point at the vortex bursting location. As the angle of attack further increases production of vorticity outgrows convection which leads to asymmetric shedding of the vortices into the flow. This shedding produces asymmetric distribution of lift that leads to wing rock. Due to the roll and yaw coupled oscillations of these unbalanced forces; delta wings encounter nose slicing and loss of control as well.

1.4 Previous Research

The flow field surrounding slender wing aircraft is dominated by the vortices created at the leading edge. The aerodynamics forces created by these vortices are nonlinearly related to the instantaneous angle of attack, sideslip angle and roll angle. They are also dependent on their rates of change and time histories. The vortical flow field is influenced by sweep angle, leading edge geometry, angle of attack and free stream conditions. Sideslip is considered the most influential of these parameters for vortex development and breakdown [10].

Vortex breakdown represents a limiting factor for the slender wing design because of its strong influence on the lift. Vortex breakdown locations have been measured by several investigations [8] [9]. It has been reported that sweep angle affects the onset angle of vortex breakdown. Sideslip effectively decreases the upwind side of the wings sweep angle and increases the downwind. An increase

in sweep leads to a delay in vortex breakdown [11], however the vortex breakdown location becomes asymmetric with increasing sideslip such that the vortex on the windward side of the wing moves closer to the apex and the vortex on the leeward side migrates further away [12].

As wing sweep is increased there is a reduction in the lift curve slope. Vorticity increases with angle of attack but at a certain point circulation decreases with increasing sweep [13]. As the breakdown location migrates toward the leading edge the lift coefficient continues to increase due to the stretching of vortices and eventually the wing stalls due to the breakdown of the vortex system.

Arena [14] attempted to correlate the position of the leading edge vortices with rolling motion during wing rock and observed that the normal position of the vortices exhibited a large hysteresis loop. Arena's work also indicated a destabilizing moment during wing rock due to the vertical and spanwise position of vortices during wing rock and is attributed to hysteresis. The breakdown of the leading edge vortices contribute to a rolling moment on the wing through asymmetry. From the results obtained by Arena, a mechanism contributing to the destabilizing moment necessary to sustain the wing rock motion appears to be the time lag in the normal vortex position on the upward-going wing. This destabilization must be stronger than the damping effects for

the roll oscillation to grow in amplitude. Time lag provides growth in the roll amplitude along with the hysteresis effect at low roll angles. As the roll angle increases the time lag becomes the major contributor to the damping of oscillation, resulting in the eventual breakdown of the vortex. This damping causes a reduction in wing rock amplitude [15].

Lowson investigated vortex position and discovered that as the length of the model increased, the breakdown location moved further downstream to approximately twice the distance from the apex. Pressure recovery over the wing due to the trailing edge governed the breakdown position [16]. This and other work performed by Cassidy [17], Falvey [18], Sarpkaya and Hall [19] all point to the existence of an adverse axial pressure gradient. These observations led Escudier to equate the axial pressure gradient for inviscid flow.

$$\left(\frac{\mathbf{dp}}{\mathbf{dx}}\right) = \left(\frac{\mathbf{dp}}{\mathbf{dx}}\right) + \boldsymbol{\rho} \int_{\mathbf{0}}^{\infty} \frac{\boldsymbol{\Gamma}}{\mathbf{r^3}} \frac{\boldsymbol{\delta\Gamma}}{\boldsymbol{\delta r}} \frac{\boldsymbol{\upsilon}}{\mathbf{u}}\, \mathbf{dr} \tag{1}$$

Considering the typical tangential velocity profile of a vortex distribution the equation becomes:

$$\left(\frac{\boldsymbol{dp}}{\boldsymbol{dx}}\right) = \left(\frac{\boldsymbol{dp}}{\boldsymbol{dx}}\right) + \frac{\boldsymbol{2\rho}}{\boldsymbol{\delta^3}} \left(\frac{\boldsymbol{\Gamma^2}}{\boldsymbol{2\pi}}\right)^{\mathbf{2}} \frac{\boldsymbol{d\delta}}{\boldsymbol{dx}}\ \boldsymbol{dr} \tag{2}$$

This equation shows that as the core of the vortex grows in size the swirl contribution is positive. The importance of the swirl contribution continues to grow as the core expands in size rapidly [20].

Using the momentum equation to analyze the upstream location of vortex breakdown, Krause showed that as the core grows in the streamwise direction the radial velocity of the vortex must increase and that this eventually leads to breakdown. He concluded that the vortex breakdown can be delayed by decreasing the maximum azimuthal velocity and increasing the freestream velocity. This work and further work done by Hall and Sarpkaya showed there were several governing parameters to breakdown but that the overall pressure gradients were extremely crucial to vortex formation and breakdown [21] [22].

1.5 Vortex Breakdown Theories

Several theories exist that attempt to explain the vortex bursting process. While much work has been done on this subject over the years, no single theory fully explains the phenomena [23]. The main problem in developing a general theory for vortex bursting is that there are several mechanisms that influence the phenomenon. Each of these mechanisms become dominant in the bursting process under specific conditions [24] [25]. Two common mechanisms are core stagnation and spiral instabilities.

1.5.1 Core Stagnation

As the angle of attack increases, the pressure gradient becomes adverse over the upper surface of the body and begins to slow down the vortex core's axial velocity. At some point the inner core velocity is no longer able to maintain constant circulation and breaks down [23].

1.5.2 Ludwieg's Spiral Instability Theory

Ludwieg proposed that vortex bursting is due primarily to spiral instabilities that grow over time. When the spiral instability's growth reaches critical amplitude it transitions into a new phase [26] [27]. This theory has been used to predict vortex bursting on slender wings but becomes inaccurate if sweep is not constant [28].

While certain circumstances exist where this spiral breakdown theory is accurate, it is unable to explain axisymmetric breakdown. Also, the conditions that this theory requires to be accurate do not exist for all cases where vortex bursting has been observed [24]

1.6 Flight Dynamic Phenomena

1.6.1 Wing Rock

Wing rock is a self sustained oscillatory mode common in many modern high performance aircraft. This phenomenon exhibits constant amplitude rolling oscillations at moderate to high angles of attack [29]. Wing rock is commonly associated with the nonlinear trend of roll damping derivatives which leads to hysteresis and sign changes of the stability parameters when increasing the angle of bank during maneuvers [30]. The delta wing is very susceptible to this oscillatory phenomenon. The wing rock motion arises from the unsteady behavior of the vortical flow fields associated with this planform. This motion is most often the result of the coupling of several degrees of freedom [13].

1.6.2 Wing Drop

Wing drop is an abrupt phenomenon that usually involves leading edge separation. As the leading edge separation expands rapidly in the spanwise direction over a small change in angle of attack it results in flow asymmetries and consequently, powerful rolling moments. One of the interesting features of wing drop is the random nature of its occurrence during what can be an identical flight maneuver [30].

1.6.3 Nose Slice

Nose slice is rapid yaw divergence that can also result in a spin departure **[31]** [32] [33]. The primary contributors to nose slicing are loss of directional stability, asymmetric yawing moments and adverse yaw. As angle of attack increases, the directional stability of an aircraft is reduced due to the fuselage wake on the vertical tail surface. Because of this reduction of directional stability the yaw moment created by the asymmetric vortices can cause the aircraft to yaw rapidly. A sketch of the asymmetric vortex position can be seen in Figure 11.

1.7 Vortex Flow Control Methods

Control of vortex flow can be accomplished by modifications to the vortex location, strength and structure. These affect the overall pressure gradient which is influences the vortex formation and breakdown. The amplitudes of vortex instability that result in wing rock can be attenuated using a variety of flow control methods. Some of the methods used to date can be divided into active and passive flow control. These flow control methods can manipulate flow separation, separated shear layer, vortex formation, flow reattachment and vortex breakdown [34].

Several control surfaces have been used to control the formation, strength and location of vortex breakdown. Gursul, Wang and Vardaki summarized the

primary methods used [34]. Two such methods are blowing/suction and unsteady excitation.

1.7.1 Blowing and Suction

Leading edge suction, blowing from small aspect ratio jets and trailing edge suction are methods that fall under this category. Since vortices form at the leading edge, control of the shear layer can be manipulated by suction or blowing in that vicinity.

The overall affect of blowing on the vortex strength is unknown, but measurements taken by Hong, Celik and Roberts indicate that completely attached flow is achievable. Blowing causes the vortices to be displaced away from the wing upper surface inducing a rolling moment for asymmetrical blowing [35]. Further work suggested that flow reattachment occurrs due to the energizing of the separated shear layer by blowing. Suction at the leading edge results in a reduction in swirl level and the overall strength of the vortex. This change forces the breakdown location further downstream [36].

Trailing edge suction and blowing alters the pressure gradient and the pressure recovery affects the bursting location as suggested by Lowson [16].

1.7.2 Unsteady Excitation

Several studies have been done to show the effect of unsteady excitations on the vortex flowfield. These generally are created by wing oscillations.

Low frequency excitations have resulted in increased vortex circulation and for certain cases resulted in a delay in vortex breakdown [37] [38]. It has been suggested that variations in the external pressure gradient generated by unsteady excitation play a major role in increased circulation and delayed bursting [39].

High frequency excitation experiments have shown evidence of performance improvements through the manipulation of the separated shear layer. However, wing sweep is a dominate parameter and the high frequency excitations have a significantly more beneficial effect on wings with low sweep angles.

1.8 Research Motivation

As the need for higher maneuverability and performance of fighter aircraft increases the understanding and alleviation of vortex bursting under dynamic and high angle of attack flight conditions becomes crucial to the development of these aircraft.

From the body of research cited in this thesis it is evident that during active wing rock and nose slicing a yawing motion is present, however to date no experimental work exists that combines the roll and yaw degrees of freedom.

To accomplish this research successfully, the following tasks or milestones were established:

The objectives of the present work were to design and build a delta wing model capable of roll, yaw and coupled roll and yaw oscillations and investigate the sideslip oscillations accurately and to determine possible flow control techniques to alleviate yaw and roll oscillations.

Chapter 2

Experimental Setup

2.1 Test Facilities

2.1.1 Wind Tunnel

Experiments were performed in the Auburn University 3 by 4 ft close circuit, low speed tunnel capable of a maximum velocity of 180 ft/s. Aerodynamic forces and moments were measured using an external 6-component pyramidal balance. Data was acquired using a National Instruments A/D board and Labview data acquisition software sampled at 500 Hz continuously.

The pyramidal balance was routinely calibrated during tests. A reduction matrix generated converted the load cell signals to aerodynamic forces and moments. The reduction matrix is given in Table 1 (Appendix B).

2.2 Model Description

The delta wing model, shown in Figure 12, had a leading edge sweep of Λ = 75 degrees, root chord of 19.688 in and a base span of 6.438 inches. The model

was machined from a 1 inch stock of solid aluminum. The center of the model was hollowed out to accommodate the yaw bearing system near the model's center of gravity. A slot was cut into the base to allow the $^3/_4$ in diameter stainless steel shaft to connect to the yaw bearing collar.

Since the model required coupled roll and yaw motion, roll - free motion was achieved with the use of a shaft that was attached internally with two roller bearings behind the model. The precision bearings allowed the model to be free in both the yaw axis and roll axis simultaneously and allowed the model to exhibit coupled motion when exposed to wind. Both roll and yaw motion could be locked out allowing the model to be configured to exhibit either motion independently or together (Figure 13).

2.2.1 Model Mounting

The model was mounted to the pyramidal balance using a dual support system with an integrated angle of attack measurement linkage. The support system was capable of manually setting the initial incidence so as to perform full $\alpha = \pm 20$ degrees only. This set up can be seen in Figure 14. A stainless steel shaft was used to attach the delta wing model to the roll bearing system. This shaft passed through a brass collar that contained two stainless steel ball bearings. An optical encoder was attached to the rear end of the shaft for the roll

measurement. The linkage system was shrouded to prevent aerodynamic loading of the support system.

2.3 Passive Flow Control Methods

The model was designed to allow for the attachment of a canard and a separate double delta wing in the aft location. The canard and double delta wing configurations were used to determine their effectiveness in controlling the roll and yaw oscillations.

2.3.1 Canard

The canard was a delta shape with a sweep $\Lambda = 50$ degrees and a root chord length 3.937 inches. The canard attachment was mounted to the top of the delta wing using three set screws. The canard configuration can be seen in Figure 15.

2.3.2 Double Delta Wing

The double delta wing was a delta shape with a sweep $\Lambda = 50$ degrees and a root chord length 7.875 inches. The double delta attachment was mounted to the aft of the delta wing using four set screws. The double delta configuration can be seen in Figure 16.

2.4 Instrumentation

2.4.1 Roll Measurements

A US Digital HB6M high resolution hollow bore optical encoder was used to measure roll motion. The encoder was slipped on the main shaft to which the main wing was mounted. The encoder was capable of tracking at up to 6,000 RPM or 2,000 cycles per revolution, a maximum acceleration of 100,000 rad/sec^2. The optical encoder was placed directly behind the model above the pyramidal balance shroud. The encoder can be seen in Figure 17 and a detailed drawing is illustrated in Figure 18. Additional details are listed in Table 2 (Appendix B).

2.4.2 Yaw Measurements

A Honeywell HC1512 sensor was used to measure yaw motion. This sensor is a high resolution magnetorresisive sensor that is capable of measuring the angle direction of a magnetic field from a magnet with < 0.07^o resolution and an angular range of ± 90 degrees. The sensor is in the form of a Wheatstone bridge and was placed directly on the mount for the yaw bearing allowing it to remain fixed with respect to the yaw motion (Figure 19). A magnet was placed externally on the model and rotated with the model with respect to the sensor. Since the sensor measured field direction versus field strength the sensor was insensitive to the temperature coefficient of the magnet and shock and vibration. The sensor

was capable of withstanding large variations in the gap between the sensor and the magnet. Leads were run from the sensor to the power supply through the model to prevent aerodynamic interference. Key features of the sensors can be seen in Figure 20 and the integrated circuit used can be seen in Figure 21. The placement of this sensor with respect to the model bearing is depicted in Figure 22. Additional features are listed in Table 3 (Appendix B).

2.5 Wind Tunnel Flow Visualization

To better understand the complex nature of the flow field, surface flow visualization was also performed. This was accomplished using a combination of kerosene, oil, oleic acid and titanium dioxide. The entire upper surface of the model was painted with the mixture to capture the flowfield in its entirety. As the kerosene evaporated, the tracer particles showed the trajectory of limiting streamlines under the vortex system. Once these streamlines were established, photographs of the model were taken and recorded for post processing.

Chapter 3

Results and Discussion

Tests were conducted at a tunnel free-stream velocity of 100 fps resulting in a Reynolds number of 550,000 based on the root chord. Force and moment data was acquired for α = 0 – 35 degrees. However, for the long time histories the range of angle of attack was changed to α = 15-35 degrees. Extended time histories for all cases were obtained at 30 degrees angle of attack. A right hand rule is used to describe the clockwise and counterclockwise motion of both wing roll and yaw, where the x-axis is aligned in the streamwise direction. Counterclockwise is positive wing roll and sideslip and clockwise is negative. Illustrations of the coordinate systems used are in Appendix C.

3.1 Fixed Wing Case

From the tine history presented in Figure 23 it is clear that the C_L increased with step changes in α. A transient of C_L spike towards the beginning of the change in α is attributed to the motion of the system responsible for setting the

angle of attack. However, only the time records without any transients were used for averaging. A close up of the time history is shown in Figure 24.

C_D exhibited a similar transients due to rapid motion of angle of attack linkage. Temporary reduction of C_D as evident in Figure 25 and is attributed to vortices moving closed to the upper surface decrease in wake size due to motion of the model. Figure 26 shows a close up o the C_D history.

Surface flow visualization showed that the first separation line (A1) originated identified near the leading edge. The primary separation point is identified in Figure 27. The primary and secondary separation lines were investigated with respect to the location of the yaw bearing and model chord centerline to establish a coordinate system for comparison. The secondary separation line (S2) was 0.892 inches from the centerline and the third separator line (S3) was 1.127 inches from the centerline. The reattachment point coincided with the centerline of the model in the plane of symmetry. Clear definition of the vortex core and bifurcation line symmetry was good indication that the two main vortices were strong and grew progressively in the streamwise direction.

3.2 Roll - Free Case

A sinusoidal variation of the coefficient of lift was observed for the roll - free case. As the roll increased, the corresponding C_L decreased indicating effect of

vortex bursting. The peak value of C_L always correlated with the zero roll location Figure 28.

Roll angles varied between $\phi = \pm 30$ degrees. The frequency of the roll motion was 3.2 Hz with a period of 0.3125 sec. Since the lift followed roll, the frequency and period of C_L were the same. A phase portrait for a typical limit cycle is shown in Figure 29. The model had a clockwise roll rate of 600 deg/sec and a counterclockwise roll rate of -700 deg/sec. This is attributed to a slight variation in mass distribution of the model Figure 30.

A similar pattern was observed for C_{SF} and C_{RM}. As the wing rolled from its neutral location to a clockwise or counterclockwise, C_{SF} and C_{RM} changed accordingly, however, with a slight lag due to inertial effects (Figure 31 and Figure 32).

From the time history of roll and the angle of attack, a low amplitude burst of roll oscillation was observed around $\alpha = 20$ degrees, followed by continuous roll oscillations around $\alpha = 23$ degrees and peaked at $\alpha = 28$ degrees (Figure 33 and Figure 34). Afterwards, the large scale roll oscillations resulted in loss of lift as evident in Figure 35, but the wing never completely stalled.

The flow visualization for the roll - free case clearly showed the first separation line (A1) and the primary separation point, identified in Figure 36. Unlike the fixed wing case, immediately following the transition zone the

thickness of the secondary separation line (S2) increased due to the wing rock. The secondary separator line (S2) was 0.713 inches from the centerline. The third separation line (S3) was 1.229 inches from the centerline. This difference in distance from centerline with the fixed wing case is attributed to the thickness of the S2 line due to oscillation. The attachment point for the roll - free case did not coincided with the centerline of the model in the plane of symmetry as was observed in the fixed wing case.

3.2 Yaw - Free Case

For this case the rolling motion was constrained and the wing was allowed to oscillate in yaw only. C_L was observed to have a higher overall magnitude when compared to the roll - free case and showed an out of phase trend as compared to the roll - free case. Secondary max and min peaks were observed in C_L and are attributed to the inertia of the modal as it reached the extreme yaw positions. Model geometry such as the thickness, sharp leading edges and bevels also contributed to the secondary peaks. During the yaw motion the actual position of the vortex on the wing surface is affected, that leads to variation in the C_L. The effect of yaw amplitude on the C_L is presented in Figure 37.

Yaw angles varied between $\beta = \pm 20$ degrees and was therefore not restricted by the model's range of motion of $\beta = \pm 25$ degrees. A phase portrait for a typical

limit cycle is shown in Figure 38. The frequency of the yawing motion was 2 Hz and a period of .5 seconds. The model exhibited a maximum yaw rate of 200 deg/sec and a minimum yaw rate of -200 deg/sec (Figure 39).

A sinusoidal pattern was also observed in C_{SF} with respect to yaw with an out of phase trend similar to C_L and is presented in Figure 40.

An onset of oscillation was also observed in the time history of yaw for varying angles of attack. Large oscillations began to occur at approximately α= 29 degrees which was higher than the roll - free case. However, with the yaw only case small oscillations began to occur significantly sooner. These oscillations of small amplitude remained consistent until the oscillation onset angle was reached, beyond which the yaw oscillations continued to grow and reached a plateau at approximately α = 30 degrees (Figure 41 and Figure 42).

C_L continued to increase with angle of attack until the C_L peaked near the onset of yaw oscillations (Figure 43). This occurs due to vortex bursting, as made evident by the yaw oscillation and a steady increase in C_D (Figure 44). This increase peaked at the onset of maximum yaw oscillation similar to the roll - free case but at much smaller magnitude.

Flow visualization showed signature of spanwise oscillatory flow due to the yawing motion. The first separation line (A1) was identified near the leading edge. The primary separation point is identified in Figure 45. Similar to the roll -

free wing case, the thickness of the secondary separation line (S2) increased due to the meandering of the vortex due to sideslip. However, unlike the roll - free case the secondary separation line (S2) was 0.830 inches from the centerline and the third separation line (S3) was 1.249 inches from centerline. The location for the S2 line was more representative of the fixed wing case. The attachment line for the Yaw case also did not coincide with the centerline of the model in the plane of symmetry and increased significantly in thickness as compared to the roll - free and fixed wing case. This drastic increase in the thickness is an indication that the bifurcation line oscillated due to rapid changes in vortex mean location as represented in the time histories. The thickness of the bifurcation line explains the large ΔC_L for the yaw - free case during oscillation.

3.4 All - Free Case

When roll and yaw were combined the overall effect on lift was far more dramatic than the other cases. With the coupled yaw-roll oscillations, C_L and roll appeared to be in phase. As the roll amplitude returned to a positive slope in the direction of a neutral roll, the yaw component lagged behind inducing secondary maximum/minimum peaks in the roll oscillation. These maximum and minimum peaks correlated directly to the maximum and minimum yaw oscillations. This is a strong indication that the energy of roll at max oscillation was transferred to

yaw, so consequently yaw lagged with respect to roll, dampening the roll oscillation (Figure 48). Yaw and roll were observed to be in phase indicating that as roll angle increased or decreased, so did yaw. This is indicated by a 45 degree slope of the Lissajous diagram, as seen in Figure 49. The phase portrait of roll showed a reduction in maximum and minimum roll as well as a dampening in the roll rate when compared to the roll - free case (Figure 50 and Figure 51) and is attributed to the sideslip contribution. The yaw phase portrait illustrated a significant decrease in maximum and minimum yaw and yaw rate and more importantly, a 90 degree phase relationship between yaw rate and yaw (Figure 52 and Figure 53).

The effect of roll - free case, yaw - free case and all - free case had on the C_L was compared. The roll - free and fixed wing case showed similar trends until the onset of oscillation angle of attack was reached and roll oscillations began. A similar trend was seen for the yaw - free case albeit with a higher C_L. At the onset of oscillation, the greatest decrease in magnitude of C_L was observed in the yaw - free case. However, the lowest value of C_L was observed for the all - free case (Figure 46). Plots of C_L vs. C_D are further indication of the loss of lift at the onset of major oscillation. As presented in Figure 47, C_D for the roll - free and all - free cases increase in a non linear fashion with respect to the yaw - free and fixed wing case.

When the rolling moment was investigated a sinusoidal pattern was also observed with respect to roll and yaw. The rolling moment was seen to lag behind the roll amplitude while the yawing moment's maximum and minimum correlated directly to the maximum and minimum of the roll amplitude for positive and negative roll, similar to the roll - free case. C_{RM} and C_{YM} lagged behind the rolling amplitude (Figure 54 and Figure 55).

When the time histories of roll and yaw were plotted for varying angles of attack, an angle for the onset of oscillation was observed. Large amplitude oscillations began to occur at approximately 28 degrees angle of attack. The roll oscillation continued to grow until it reached a plateau at approximately 30 degrees (Figure 56). This was similar to the roll - free case with one exception, i.e. the maximum magnitude of roll oscillation decreased for the all - free case. The lowest value of C_L was observed for the all - free case at the onset of the yaw-roll coupled oscillations; C_L did not increase while C_D continued to increase. This trend was observed for all test cases and is presented in Figure 57 and Figure 58.

Flow visualization results indentify the primary separation point for the all - free case (Figure 59). Similar to the roll - free case, the thickness of the secondary separation line (S2) increased due to the oscillation of the vortex mean position. The secondary separation line (S2) was 0.939 inches from the centerline. The third separation line (S3) was 1.40 inches from the centerline. This difference in

distance when compared to the roll - free case is misleading since for the all - free case there is a distance increase in distance at the point of measurement. This is primarily due to the oscillation contribution causing an additional separation point (A2). The bifurcation point for the all - free case no long coincided with the centerline of the model in the plane of symmetry and presented a trend similar to the roll - free case as roll is the primary contributor to the oscillation in the all - free case.

3.5 Canard Attachment

When a short delta wing was attached near the apex of the main wing an increase in C_L was observed. However, a higher magnitude of C_L was observed for the canard (Figure 60). A significant increase in C_D was also observed (Figure 61). "Spikes" in C_L due to the motion of the model were also observed and were similar to previous cases. A larger local increase in C_L indicated that the vortices were able to attach longer due to the additional surface area. The migration of the vortices can be seen on the canard in the flow visualization images (Figure 63). The presence of the canard and an additional increase in C_D caused a drastic damping of roll oscillations reducing the roll to approximately $\phi = \pm 6$ degrees. The time history of C_L and wing rock for the canard attachment showed a similar trend to the roll - free case, with a damped roll oscillation (Figure 62).

3.6 Double Delta Attachment

An increase in C_L was observed for the double delta wing similar to the previous test cases but was higher than the canard (Figure 64 and Figure 65). Flow visualization revealed that unlike the canard, the double delta indicated a clear bifurcation line symmetrically down the model centerline. Also, seen at the leading edge where the sweep angle was reduced, was a reattachment line of the vortex (Figure 67). This outward migration of the vortex provided the additional increase in C_L compared to the base line cases. While this configuration provided the vortex with an attachment point for migration, the additional wing area increased the C_D. This combination damped the roll even further than the canard to approximately $\phi = \pm 3$ degrees (Figure 66).

3.7 Canard and Double Delta Attachment

An increase in the magnitude of C_L and C_D was observed in comparison to the double delta and canard (Figure 68 and Figure 69). Migration of the vortex near the leading edge was seen on the canard and at the leading edge where the sweep angle was reduced was a reattachment line of the vortex (Figure 67). The combination of these two attachments damped the roll completely ($\phi = \pm 0$ degrees). The C_L vs. angle of attack comparison for all flow attachments can be seen in Figure 71.

Chapter 4

Conclusions

The aerodynamics of a slender delta wing undergoing a roll, yaw and coupled roll-yaw oscillation was investigated in a wind tunnel. A strong coupling between the roll and yaw motion was observed. An angle of attack for the onset of oscillation for each individual test case was observed.

For the roll - free, yaw - free and all - free test cases, the model established a self-sustaining limit cycle oscillation. Roll oscillations compared well with Nelson's [40] with roll amplitudes of approximately $\phi = \pm 35$ degrees validating the roll measurement techniques. Slight Differences in the roll magnitude are attributed to model weight differences and the thickness of the model. Since the model used in these experiments had a larger thickness and beveled leading edge, the formation of the vortices was accordingly affected.

The yaw-roll coupling caused a sinusoidal oscillation in C_L. This oscillation was similar to the oscillation seen in the roll - free case. While the yaw - free case had secondary peaks in C_L this trend was not exhibited in the all - free case. The

overall magnitude of the yaw and roll oscillation was reduced by the coupling. Yaw was observed to have a 75% reduction in maximum oscillation amplitude for the all - free case when compared to the yaw - free case. The roll was observed to have a 20% reduction in maximum oscillation amplitude when compared to the roll - free case. This is a strong indication that the major contributor to the variations in C_L was the roll oscillation.

The lift curve versus angle of attack graph indicated that yaw-roll coupling decreased the overall C_L produced when compared to the roll - free, yaw - free and fixed wing cases. C_L vs. C_D further indicated the loss of lift at the onset of major oscillation. C_D for the roll - free and all - free cases increased in non-linearly compared to the yaw - free and fixed wing case. The fixed wing case presented the most linear C_L versus C_D case when compared to all other test cases.

A significant reduction in roll oscillation was observed for all passive flow control configurations. With the combination of the canard and double delta wing rock was completely eliminated. A significant increase in C_D was measured. The all - free case, canard and the double delta configuration damped the roll. The only contributor to the roll damping in the all - free case was the yaw contribution. This self sustaining limit cycle showed a damping with the yaw-roll

coupling effect. The canard and double delta would be the more favorable flow control devices to control roll oscillation.

In summary, the following conclusions are drawn;

1.) If allowed to oscillate, a slender delta wing will enter a self sustaining limit cycle for roll and yaw separately. This limit cycle will increase in amplitude over a short period of time until it reaches maximum amplitude.

2.) Yaw oscillation reduces the average value of C_L and is primarily due to the motion of oscillation being parallel to the migration of the vortex as they burst down.

3.) The all - free case produced the lowest values of C_L. This was due to the overall instability of the model oscillation simultaneously in two degrees of freedom.

4.) For the roll - free and all - free cases C_L varies in phase with roll. However, unlike the roll - free case, the all - free case presented secondary maximum and minimum peaks in C_L. These peaks correlated directly to the maximum and minimum peaks in the yaw motion. This correlation indicates that the yaw motion slightly dampens the roll oscillation. This is accomplished by transferring roll inertial energy into yaw.

5.) The canard attachment to the slender delta wing increased both C_L and C_D and also provided a surface for vortex attachment whcih resulted in a damping of roll oscillations ($\phi = \pm 6$ degrees).

6.) The double delta configuration also increased both C_L and C_D more than the canard. A clear vortex core migration was established at the leading edge where the sweep decreased. This attachment also reduced the overall roll oscillation significantly ($\phi = \pm 3$ degrees).

7.) The combination of canard and double delta configurations showed a further increase in both C_L and C_D and reduced the roll completely ($\phi = \pm 0$ degrees) with a drastic increase in C_D as compared to all other test cases.

Chapter 5

Recommendation

Since the focus of this work was the aerodynamic forces associated with roll, yaw and coupled oscillations; a lighter model would be extremely beneficial. During balancing of the model, it was difficult to achieve balance for both the roll and the yaw cases simultaneously. Since the model was hollowed out to allow for an internal bearing system the only weight in the model was along the outer edge and at the nose. This weight caused uneven balancing along the roll axis and primarily for the yaw axis. This problem could be reduced by constructing a model made from a lighter material than aluminum.

The angle for the onset of instability could be further investigated using a more sensitive angle of attack measurement system. The angle of attack was measured by an accelerometer, the roll and yaw oscillations decreased the accuracy of the angle of attack measurements. The accuracy of the accelerometer used was ± 1 degree.

References

[1] J. D. Anderson, *Fundamentals of Aerodynamics*, McGraw-Hill, 1991.

[2] I. Heron, "Vortex Burst behavior of a Dynamically Pitched delta Wing Under the Influence of a von Karman Vortex Sheet and Unsteady Freestream," Wichita State University, 1997, Doctors Dissertation.

[3] R. A. Sprague, "Wind Tunnel and Water Channel High Angle of Attack Delta Wing Study and Comparisons, with Particular reference to Vortex Core and Burst Locations," Wichita State University, 1989, Masters Thesis.

[4] J. D. Anderson, *Fundamentals of Aerodynamics, 4th ed.*, McGraw-Hill, 2007.

[5] B. W. McCormic, *Aerodynamics, Aeronautics and Flight Mechanics*, Wiley, 1979.

[6] M. Lee and C. M. Ho, "Lift Force of Delta Wings," *Applied Mechanics Review*, Vol. 43, No. 9, September 1990, pp. 209-221.

[7] L. Sidney, "The Structure of Vortex Breakdown," *Ann. Rev. Fluid Mech*, 1978, pp. 221-46.

[8] J. H. Leibovich and S. Faler, "Distrupted States of Vortex Flow and Vortex Breakdown," *Physics of Fluids*, Vol. 20, September 1977, pp. 1385-1400.

[9] J. Bornstein and M. P. Escudier, "LDA Measurements within a Vortex Breakdown Bubble," *International Symposium on Applications of Laser-Doppler Anemometry to Fluid Mechanics*, July 5-7, 1982, pp. 10.3.1-10.3.11, Fluid Mechanics and Heat Transfer.

[10] K. Y. Lee and M. H. Sohn, "The Vortical flow Field of Delta Wing with Leading Edge Extension," *KSME International Journal*, Vol. 17, No. 6, 2003, pp. 914-924.

[11] N. G. Verhaagen, "Effect of Sideslip on the flow over a 65-deg Delta Wing; Final Report," 1999.

[12] D. Hummel, "On the Vortex formation Over a Slender Wing at Large Angles of Incidence," *AGARD-CP-247*, 1978, pp. 15.1-15.17.

[13] R. C. Nelson and A. Pelletier, "The Unsteady Aerodynamics of Slender Wings and Aircraft Undergoing Large Amplitude Maneuvers," *Progress in Aerospace Sciences*, Vol. 39, 2003, pp. 185-248.

[14] A. Arena Jr, "An experimental study of the nonlinear wing rock phenomenon," University of Notre Dame, 1990, Masters Thesis.

[15] A. Arena Jr, "An experimental and computational investigation of slender wings undergoing wing rock," University of Notre Dame, 1992, Doctors Disertation.

[16] M. Lowson, "Some experiments with vortex breakdown," *J. Royal Aero Soc.*, No. 8, 1964, pp. 343-346.

[17] J. J. Cassidy and H. T. Falvey, "Ovservations of unsteady flow arising after vortex breakdown," *journal of Fluid Mechanics*, Vol. 41, No. 04, 1970.

[18] T. Sarpkaya, "On stationary and traveling vortex breakdowns," *Journal of Fluid Mechanics*, Vol. 45, No. 03, 1971, pp. 545-559.

[19] M. G. Hall, *A new approach to vortex breakdown*, Proceedings of the Heat Transactions and Fluid Mechanics Institude, Stanford, 1967.

[20] L. D. Smoot, D. G. Sloan, and P. J. Smith, "Modeling of swirl in turbulent flow systems," *Progress in Energy and Combustion Science*, Vol. 12, No. 03, 1986, pp. 163-250.

[21] M. G. Hall, "Vortex Breakdown," *Annual Review of Fluid Mechanics*, Vol. 4, January 1972, pp. 195-218.

[22] T. Sarpkaya, "Effects of the adverse pressure gradient on vortex breakdown," *AIAA Journal*, Vol. 12, No. 5, 1974, pp. 602-607.

[23] K. E. Stifle and R. L. Paton, "Experiments Concerning The Theories of Vortex Breakdown," *Aerospace Science Metting*, AIAA 91-0736, Reno, 1991, p. 22.

[24] S. Leibovich, "Vortex stability and breakdowns: survey and extension," *AIAA journal*, Vol. 22, No. 9, 1984, pp. 1192-1206.

[25] T. Sarpkaya, "Vortex breakdown in swirling conical flows," *AIAA J.*, Vol. 9, 1971, pp. 1792-1799.

[26] E. H. Wedemeyer, "Vortex breakdown," High Angle of Attack Aerodynamics, AGARD 121, 1982.

[27] E. H. Wedemeyer, "Stable and unstable vortex seperation," High Angle of Attack Aerodnyamics, AGARD, 1979.

[28] F. M. White, *Viscous Fluid Flow, 2nd ed.*, McGraw-Hill, 1991.

[29] G. Guglieri and F. Quagliotti, "Experimental observation and discussion of the wing rock phenomenon," *Aerospace Science and Technology*, Vol. 1, No. 2, 1997, pp. 111-123.

[30] K. Orlik-Ruckermann, "Aerodynamic aspects of aircraft dynamics at high angles of attack," *Journal of Aircraft*, Vol. 20, No. 9, September 1983, pp. 737-752.

[31] L. Anglin E., B. Jr., and J. R. Chambers, "Effects of a pointed nose on spin characteristics of a figher airplane model including correlation with theoretical calculations," NASA TN D-5921, 1970.

[32] W. P. Gilbert, J. R. Chambers, and S. B. Grafton, "Results of resent NASA stidies on spin resistance. Stall/spin problems of military aircraft," AGARD-CP-199, 1976.

[33] J. Coe, Chambers, and W. Letko, "Asymmetric latera-directional characteristics of pointed bodies of revolution at high angles of attack," NASA TN D-7095, 1972.

[34] I. Gursul and E. V. Wang, "Review of Flow Control Mechanisms of Leading-Edge Vortices," *Progress in Aerospace Sciences*, Vol. 43, No. 7-8, 2007, pp. 246-270.

[35] J. S. Hing, Z. . Celik, and L. Roberts, "Effects of leading edge lateral blowing on delta wing aerodynamics," *AIAA Journal*, Vol. 34, No. 12, 1996, pp. 2471-2478.

[36] S. McComick and I. Gursul, "Effect of shear layer control on leading edge vortices," *Journal of Aircraft*, Vol. 33, No. 6, 1996, pp. 1087-1093.

[37] G. R. Spedding, T. Maxworthy, and E. Rignot, "Unsteady vortex flows over delta wings," *Proceedings of the Second AFOSR Workshop on Unsteady and Separated Flow*, 1987.

[38] Q. Deng and I. Gursul, "Vortex breakdown over a delta wing with oscillating leading edge-flaps," *Experiments in Fluids*, Vol. 23, No. 4, 1997, pp. 347-352.

[39] H. Yang and I. Gursul, "Vortex Breakdown Over Unsteady Delta Wings and Its Control," CINCINNATI UNIV OH, 1995, ADA304465.

[40] M. D. Nelson, "An experimental investigation of leading edge vortical flow about a delta wing during wing rock," 1991.

[41] J. D. Anderson, *Aircraft performance and design*, McGraw-Hill, Inc., New York, 1999.

[42] Wikipedia, *http://en.wikipedia.org/wiki/Mikoyan-Gurevich_MiG-21*, April 11, 2011.

[43] Wikipedia, *http://en.wikipedia.org/wiki/Convair_F-102_Delta_Dagger.*, April 11, 2011.

[44] Wikipedia, *http://en.wikipedia.org/wiki/B-58_Hustler*, April 11, 2011.

[45] L. K. Laurence, *Quest for Performance. The Evolution of Modern Aircraft*, National Aeronautics and Space Administration, 1985.

[46] N. C. Lambourne and D. W. Bryer, "The bursting of leading-edge vortices - some observations and discussions of the phenomenon," Reports and Memoranda 3282, 1962.

[47] B. W. McCormic, *Aerodynamics, Aeronautics and Flight Mechanics*, Wiley, 1979.

[48] "Hollow Bore (Hollow Shaft / Thru-bore) Optical Encoder - HB6M,".

[49] Honeywell, *www.ssec.honeywell.com*, April 11, 2011.

Figures

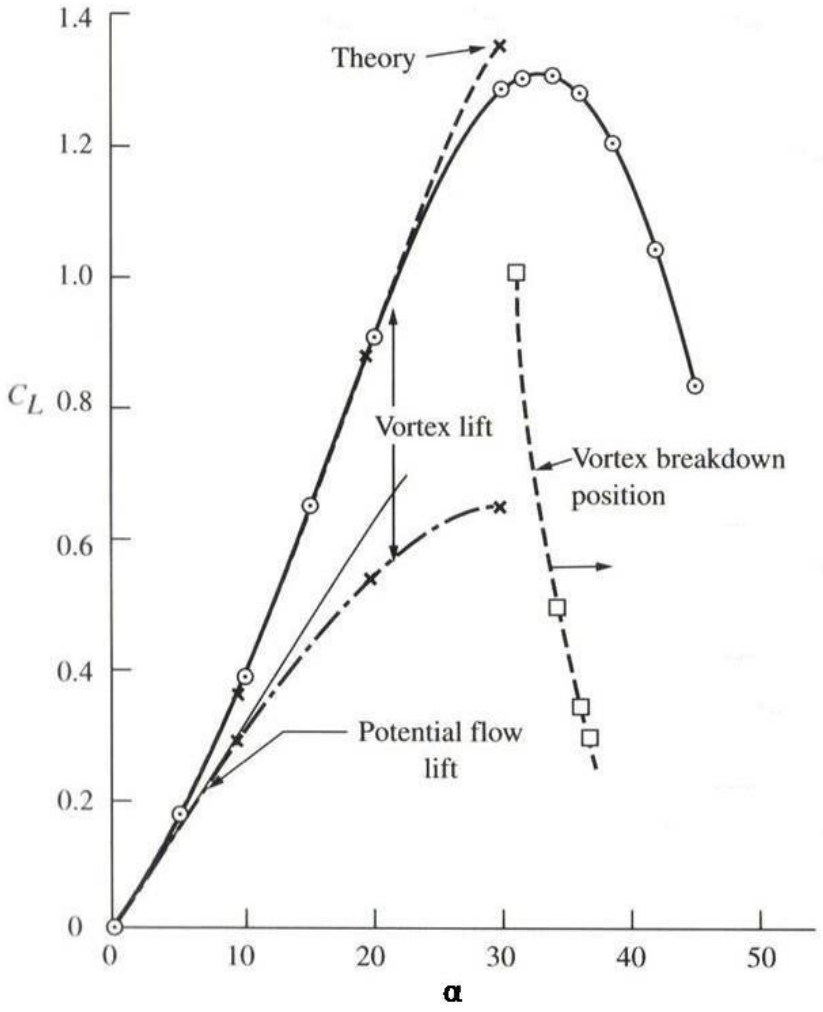

Figure 1: Coefficient of lift versus angle of attack for a classical delta wing [41]

Figure 2: Mig 21 [42]

Figure 3: Convair F-102A [43]

Figure 4: B-58 Hustler [44]

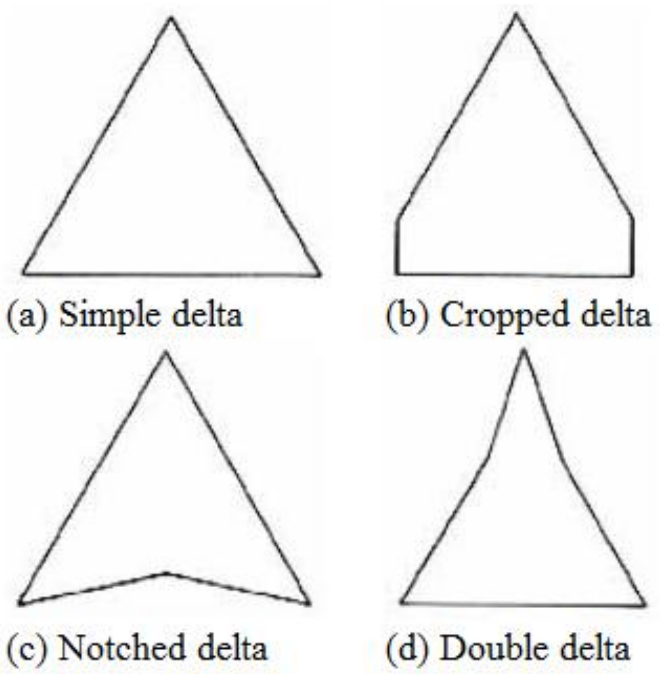

Figure 5: Primary versions of the delta wing platform [45]

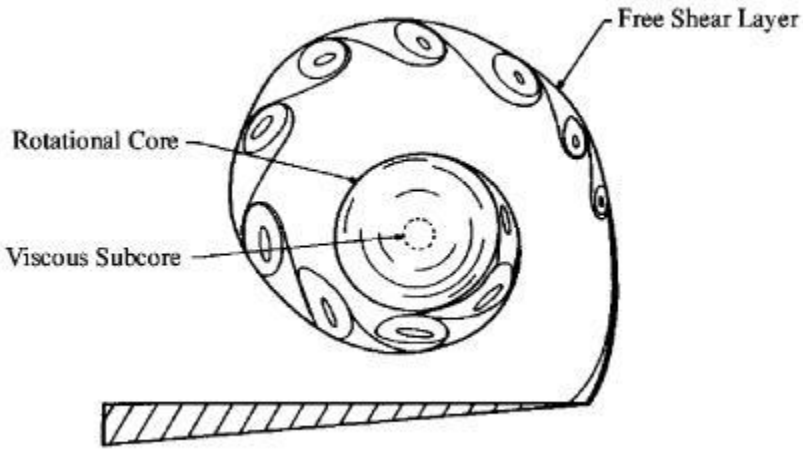

Figure 6: Detachment of flow along the leading edge [13]

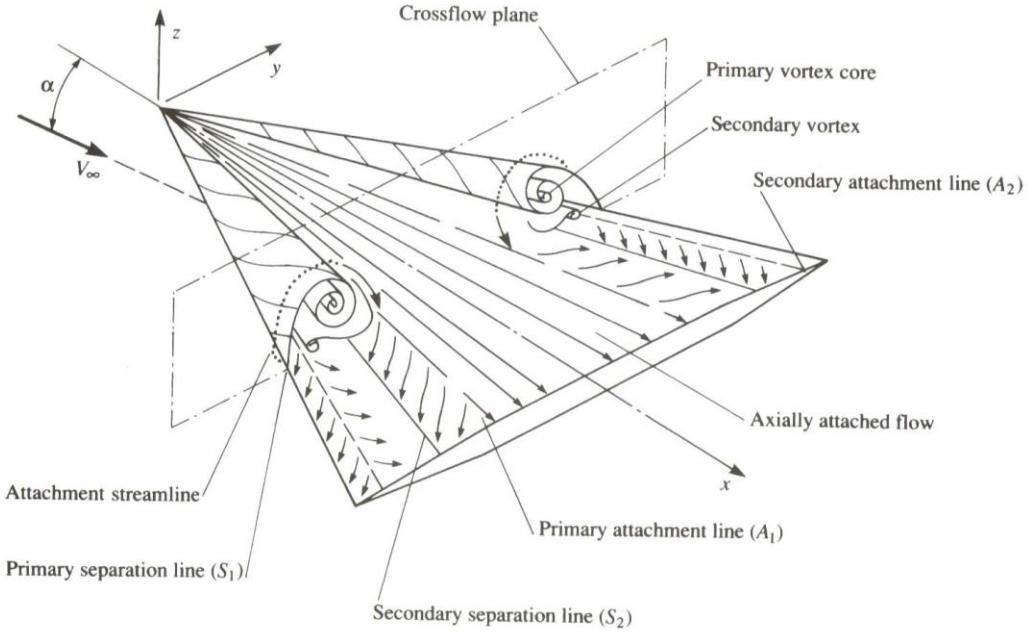

Figure 7: Topology of flow over a delta wing [1]

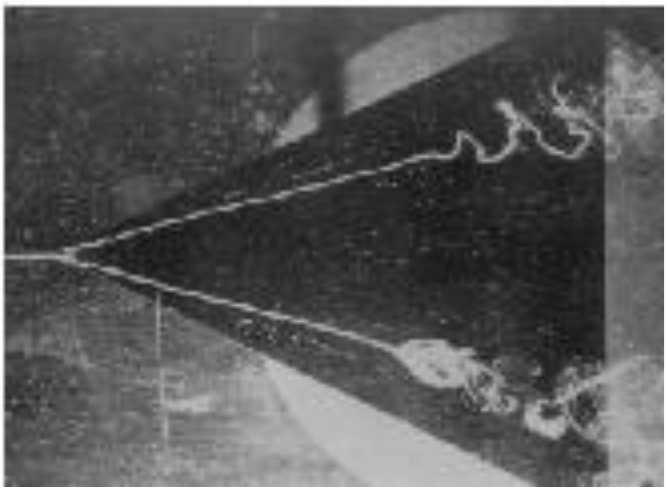

Figure 8: Spiral and bubble type bursting [46]

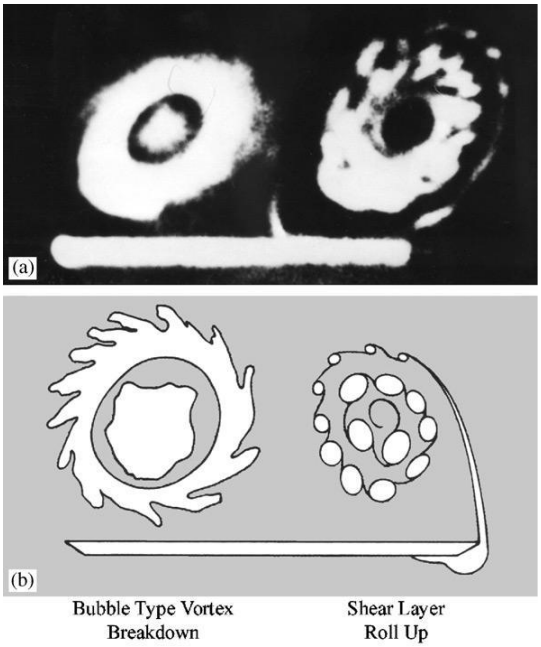

Figure 9: Bubble Type Bursting [13]

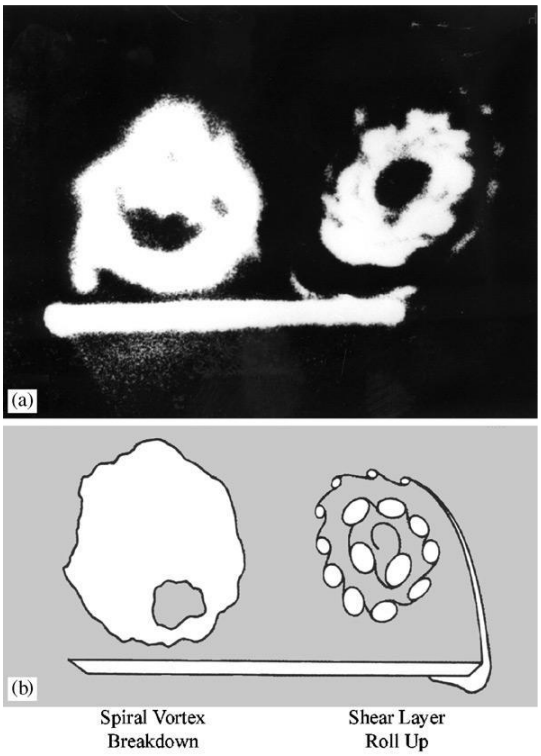

Figure 10: Spiral Type Bursting [13]

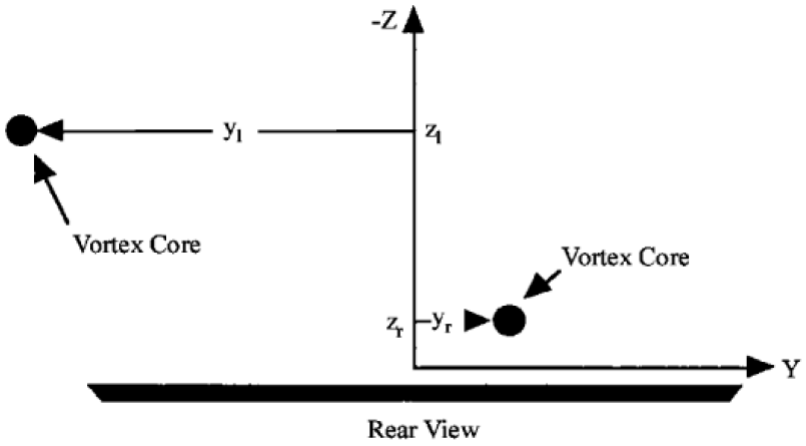

Figure 11: Asymmetric vortex position [47]

Figure 12: Delta wing model

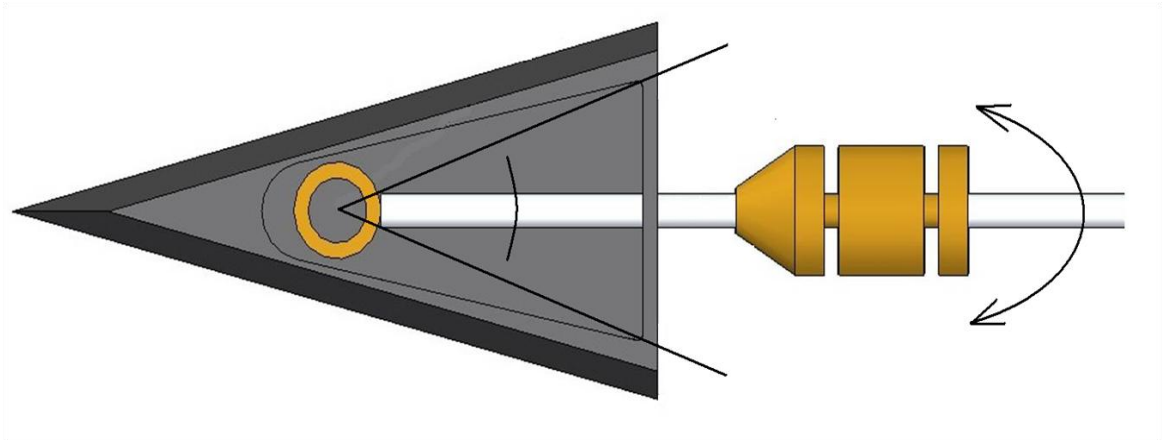

Figure 13: Delta wing model

Figure 14: Mounting System

Figure 15: Canard configuration on delta wing

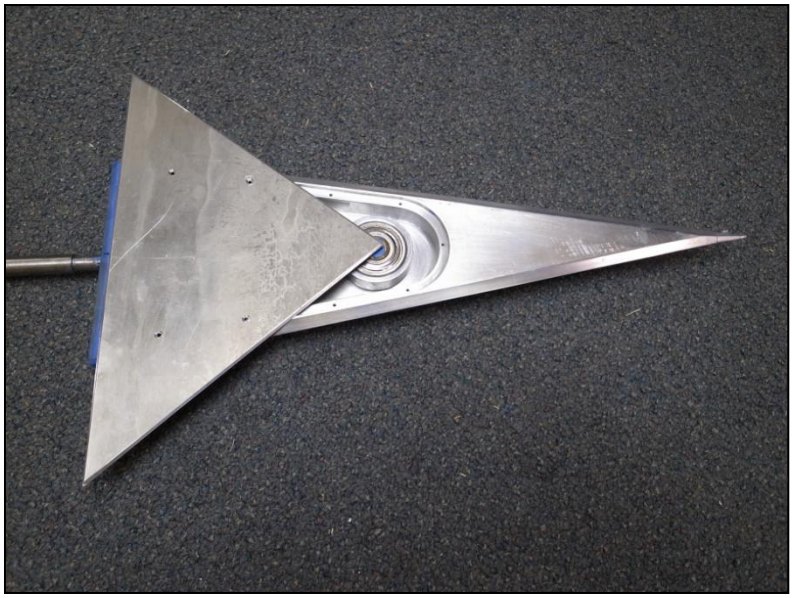

Figure 16: Double delta wing configuration on delta wing

Figure 17: Us Digital HB6M Optical Encoder [48]

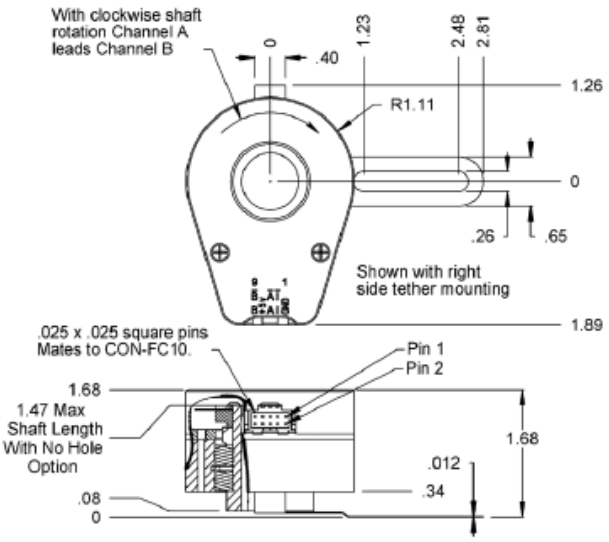

Figure 18: Optical Encoder [48]

HMC1512

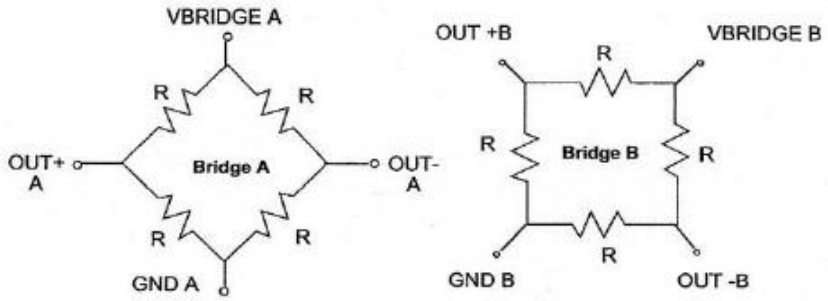

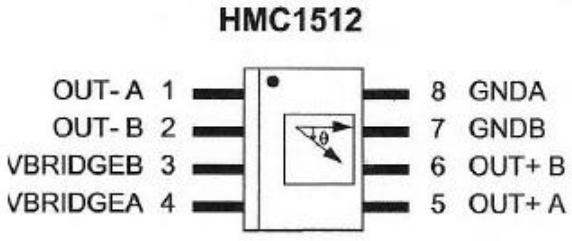

Figure 19: Honeywell HC1512 sensor schematic diagram [49]

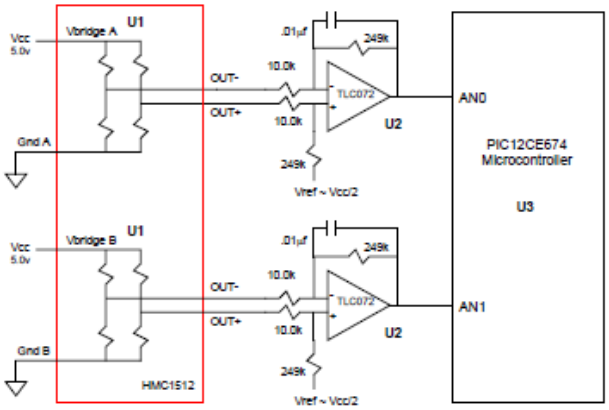

Figure 20: Honeywell HC1512 sensor circuit board [49]

Figure 21: Honeywell HC1512 sensor [49]

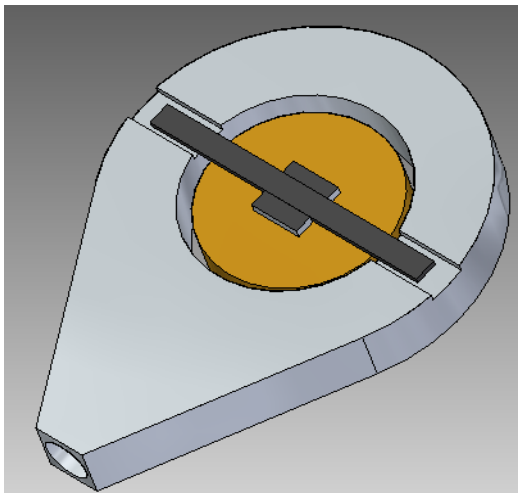

Figure 22: HC1512 sensor placement

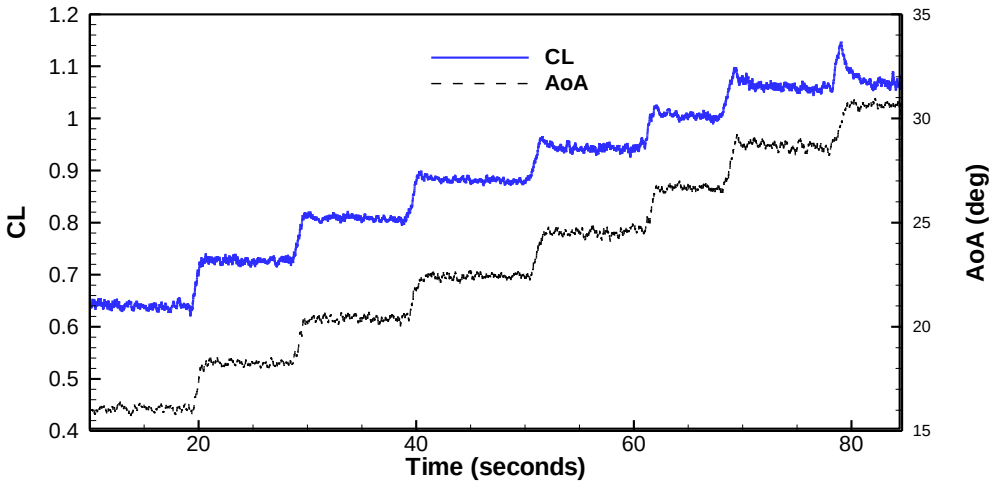

Figure 23: Time history of Lift and AoA – fixed wing case

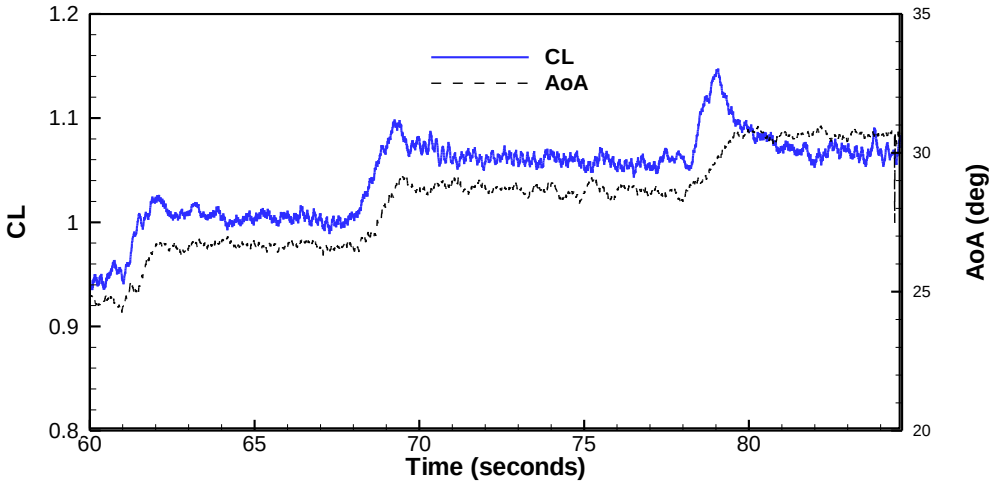

Figure 24: Time history of Lift and AoA expanded – fixed wing case

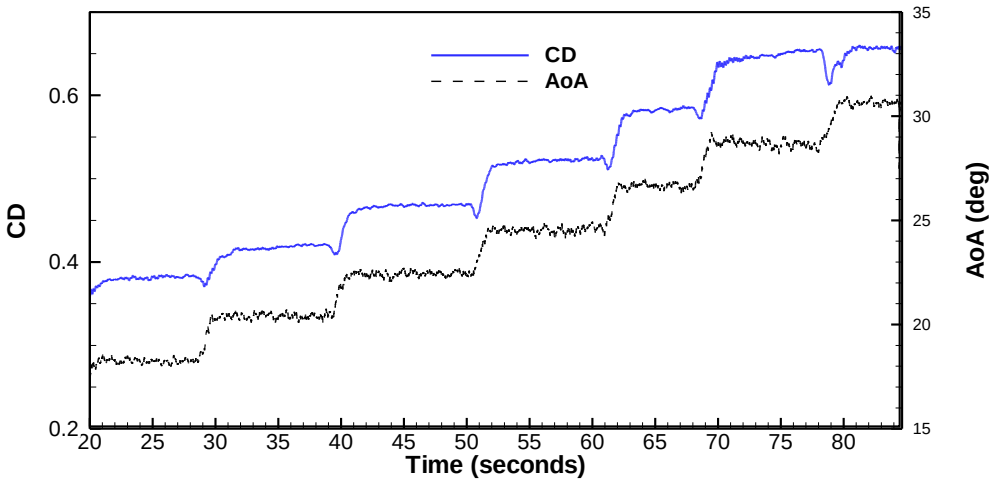

Figure 25: Time history of Drag and AoA – fixed wing case

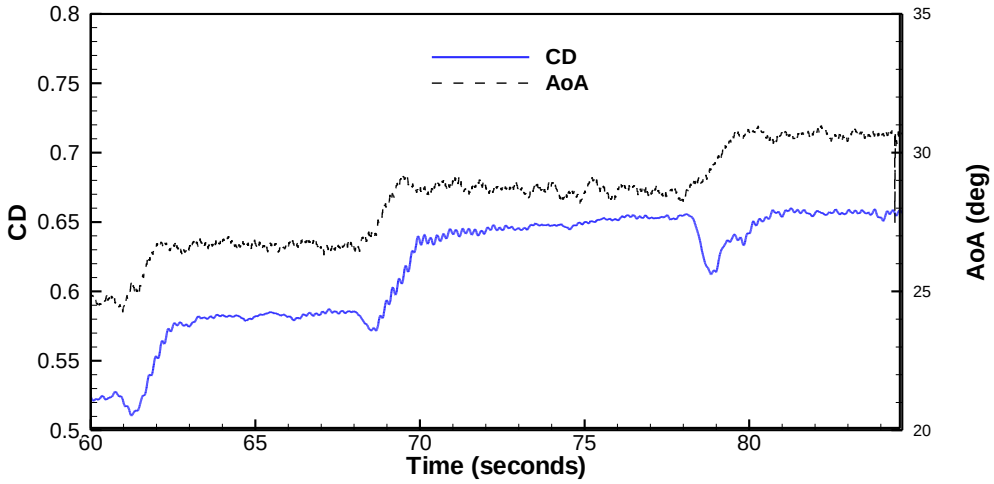

Figure 26: Time history of Drag and AoA expanded – fixed wing case

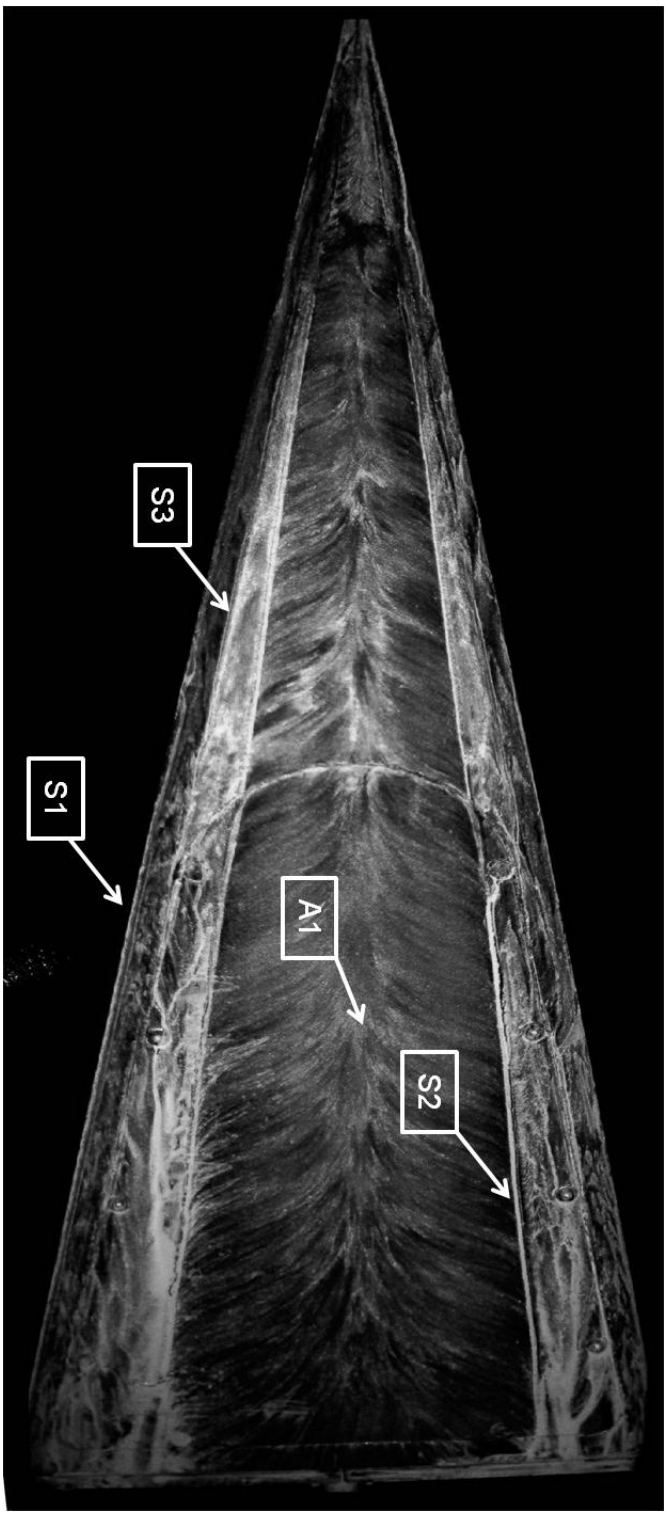

Figure 27: Fixed wing case flow visualization

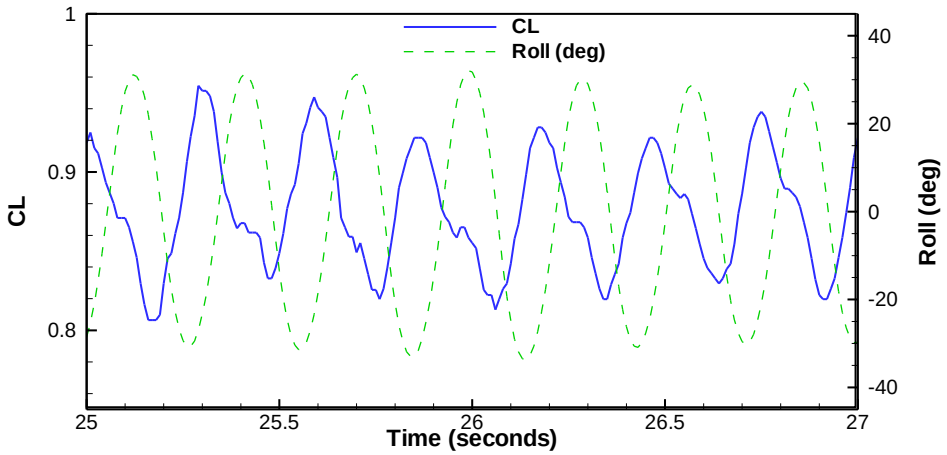

Figure 28: Time history of Lift and wing roll – roll - free case

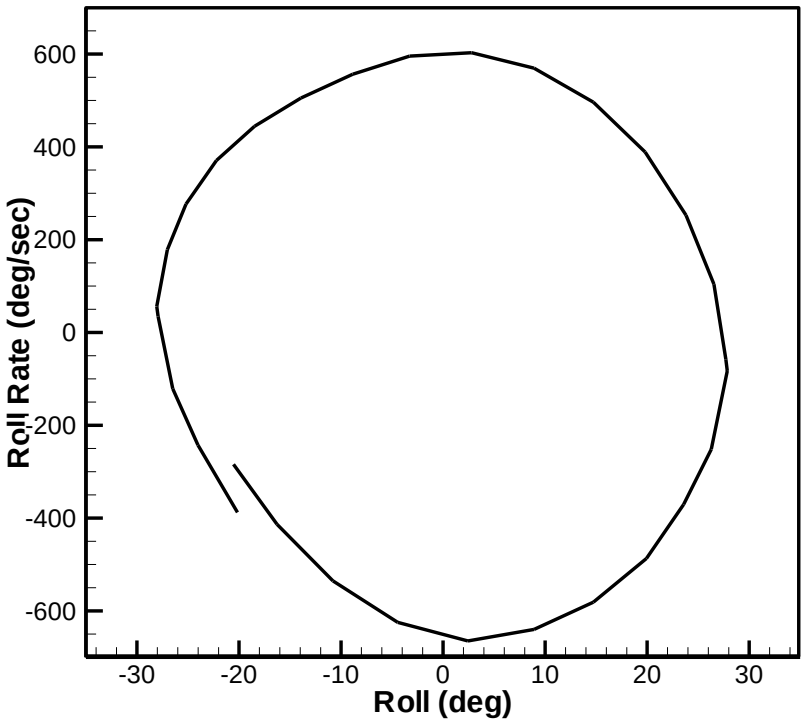

Figure 29: Phase Portrait of Roll – roll - free case

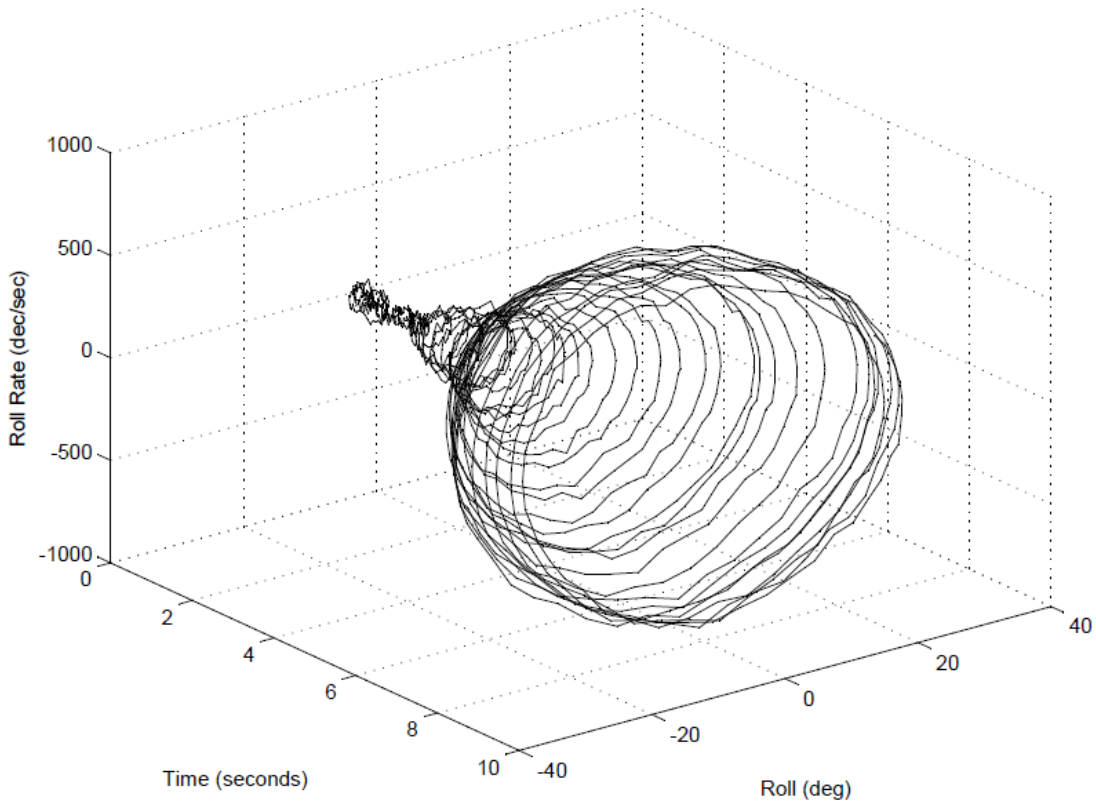

Figure 30: Extended Phase Portrait – roll - free case

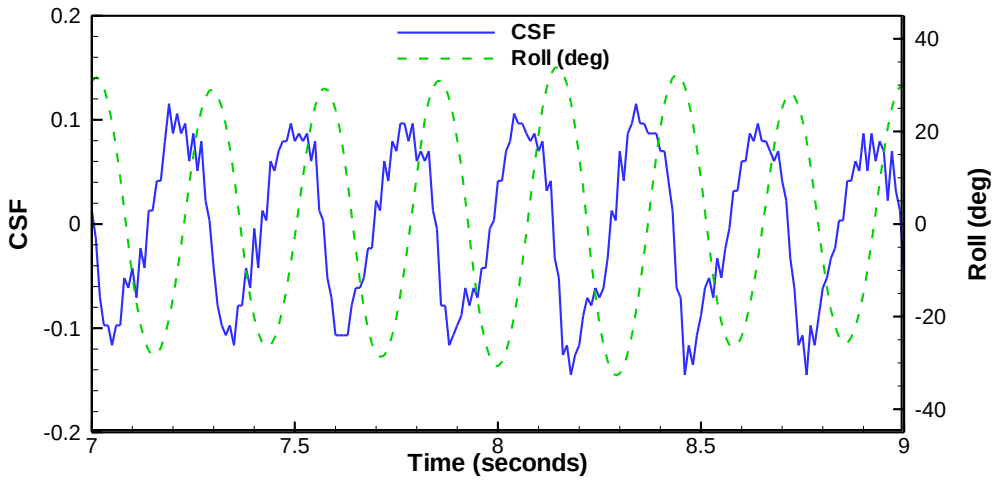

Figure 31: Time history of Side Force and wing roll – roll - free case

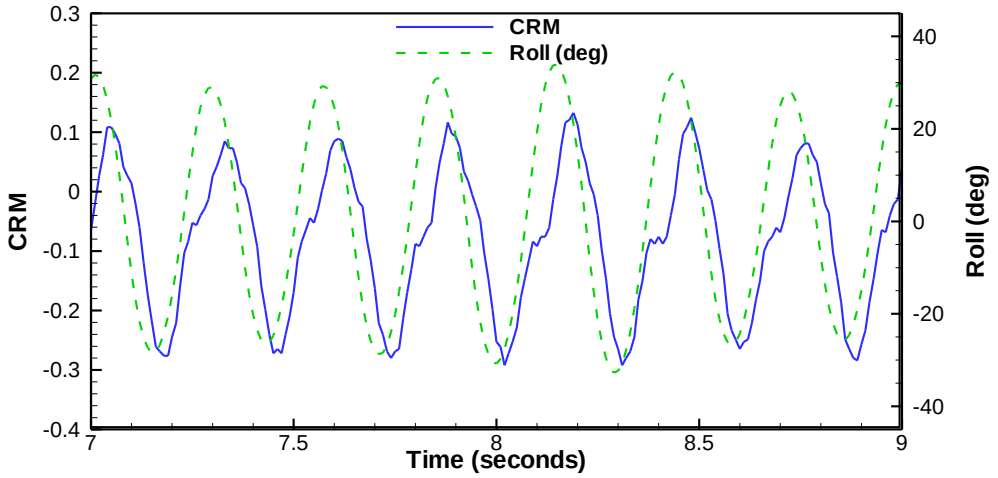

Figure 32: Time history of Rolling Moment and wing roll – roll - free case

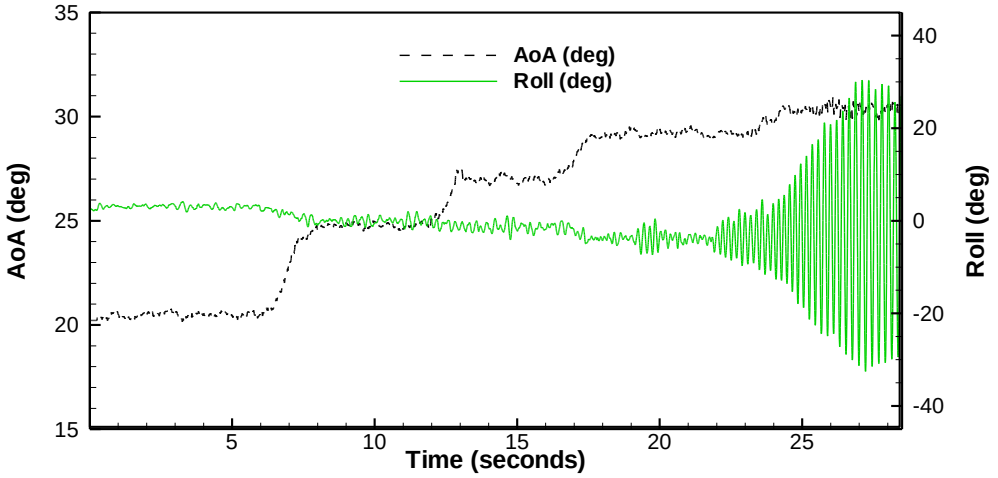

Figure 33: Time history of wing roll – roll - free case

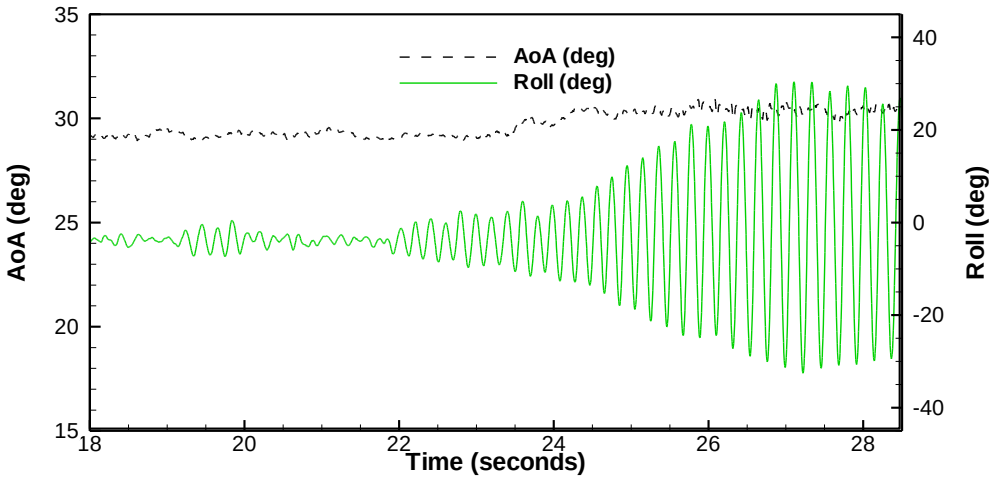

Figure 34: Roll and AoA vs. Time expanded –roll - free case

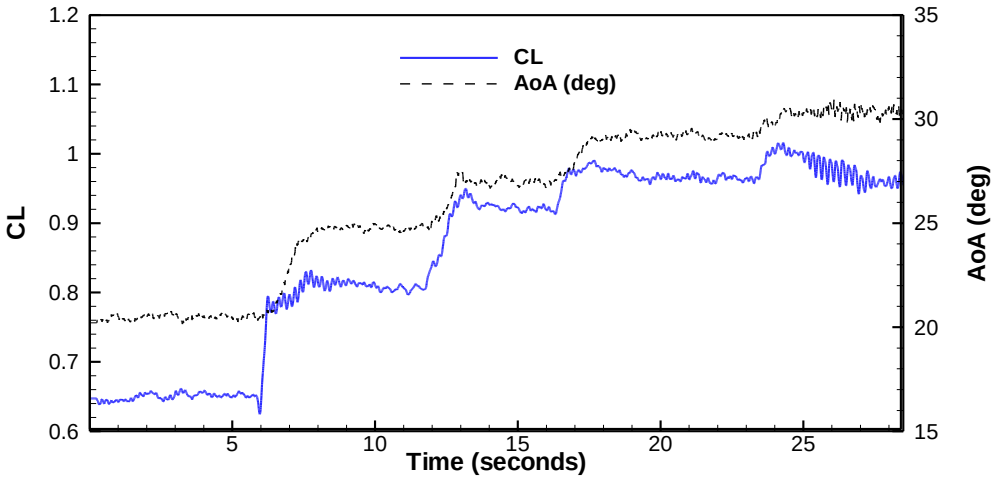

Figure 35: Time history of Lift and wing roll – roll - free case

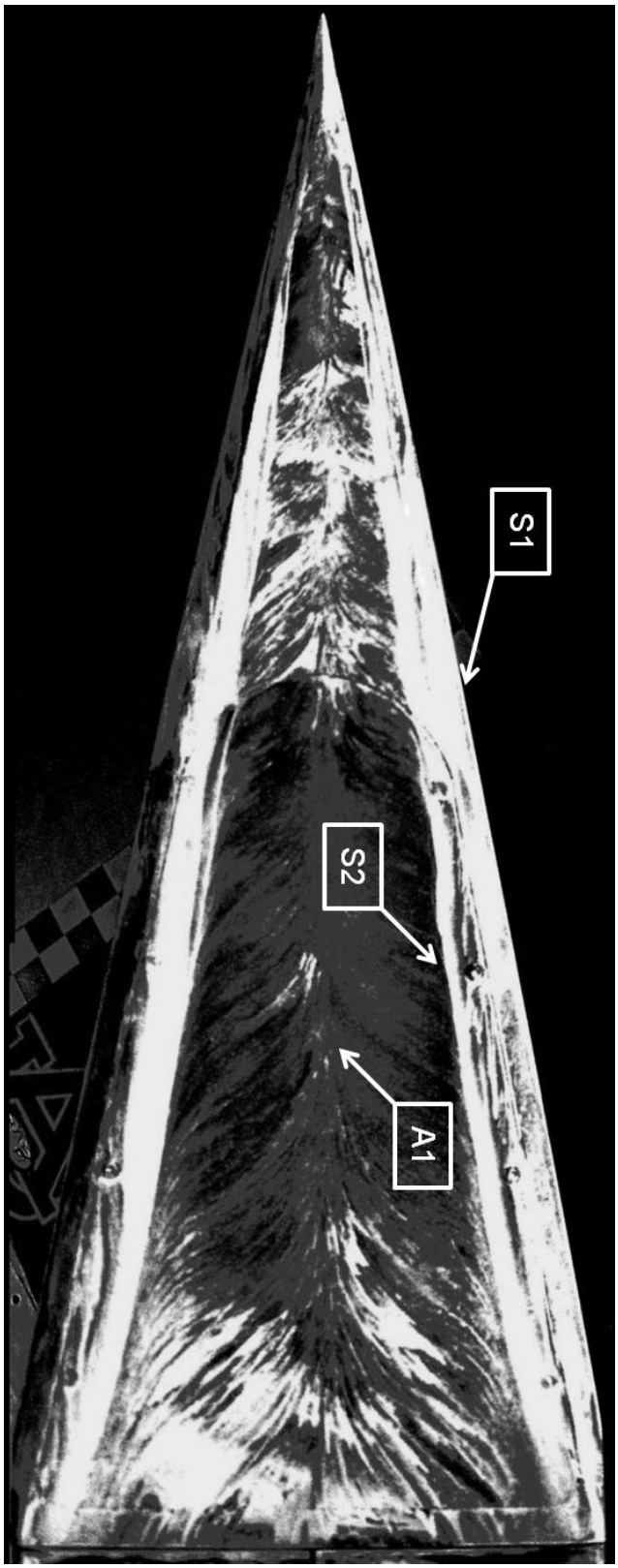

Figure 36: Roll - free case flow visualization

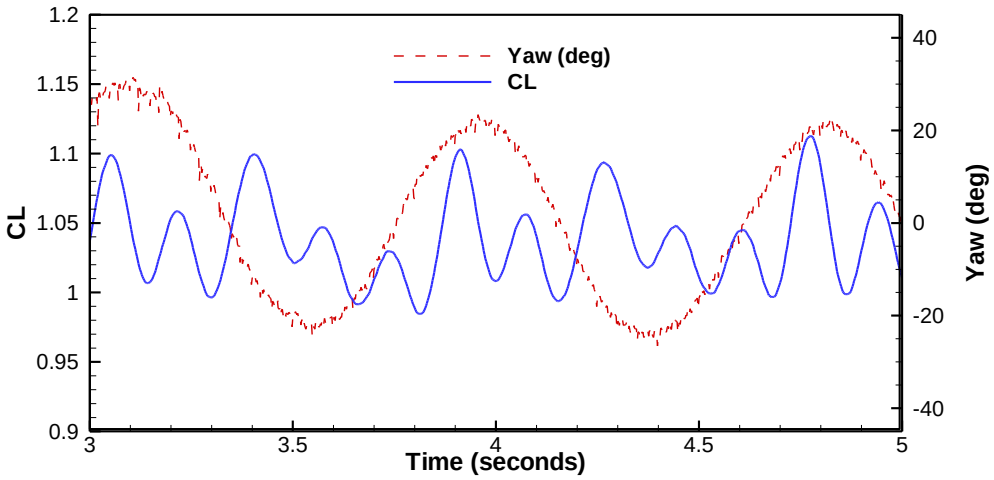

Figure 37: Time history of Lift and side slip – yaw - free case

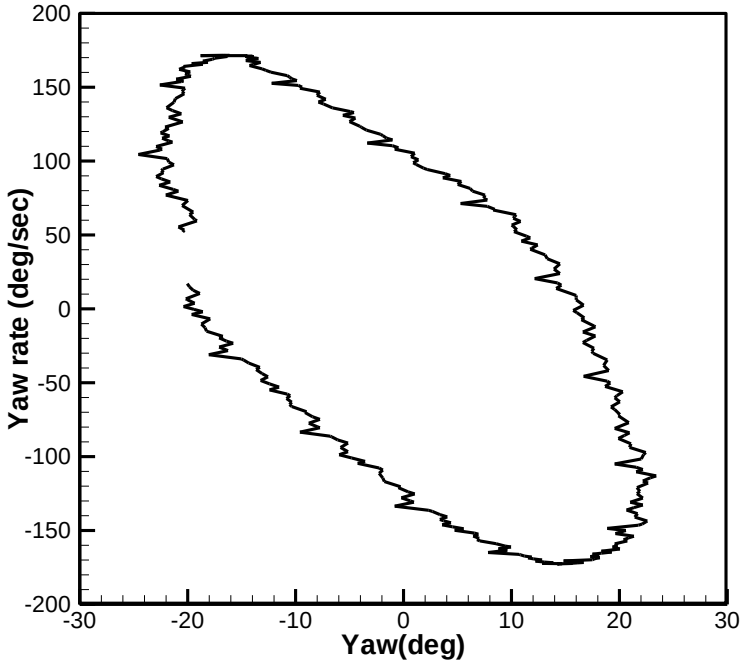

Figure 38: Phase Portrait of Yaw – yaw - free case

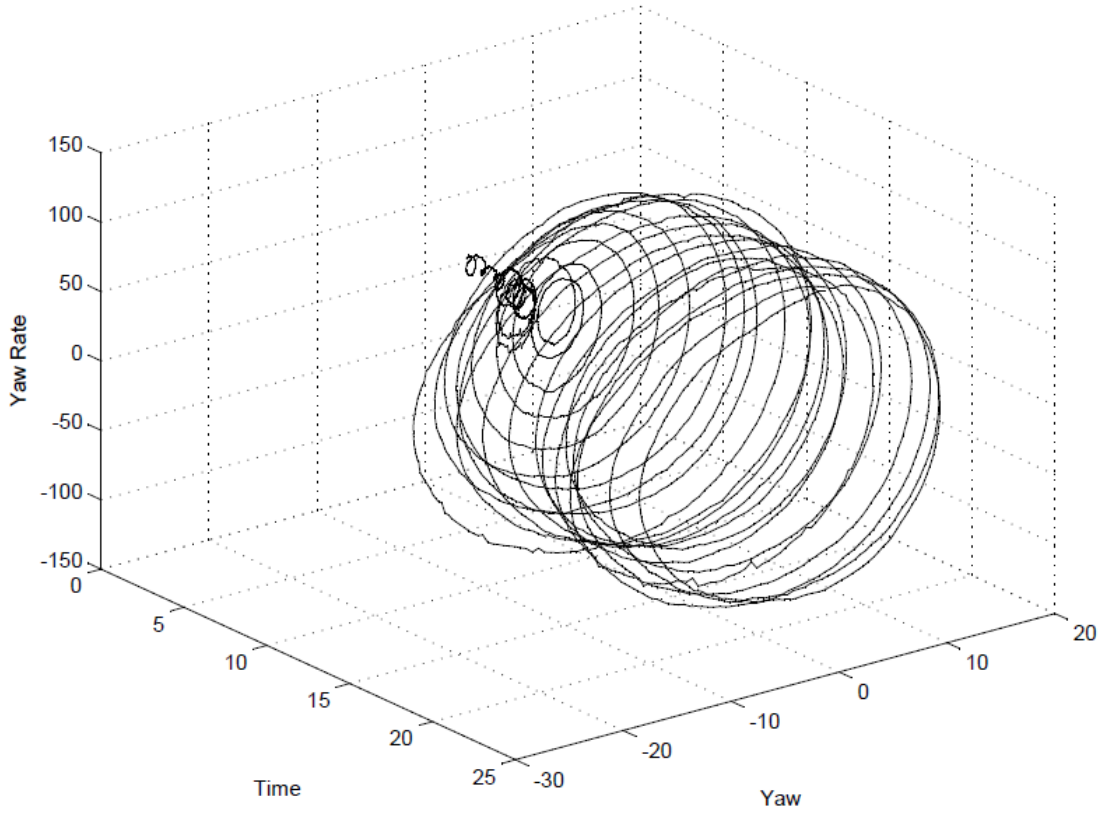

Figure 39: Extended Phase Portrait – yaw - free case

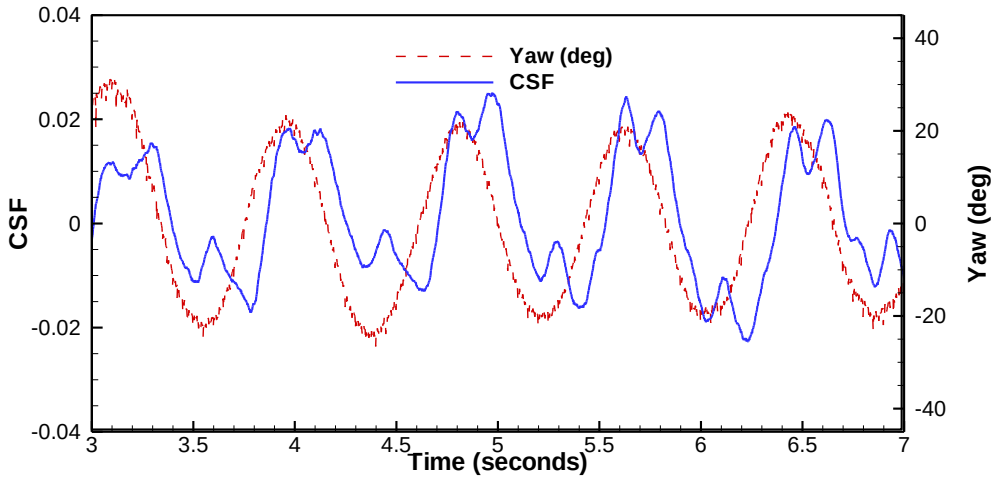

Figure 40: Time history of Side Force and side slip – yaw - free case

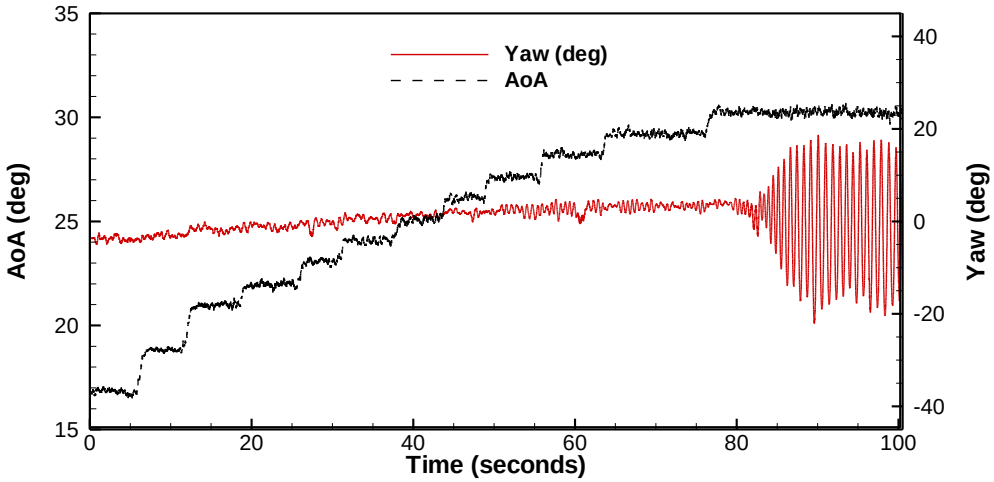

Figure 41: Time history of side slip – yaw - free case

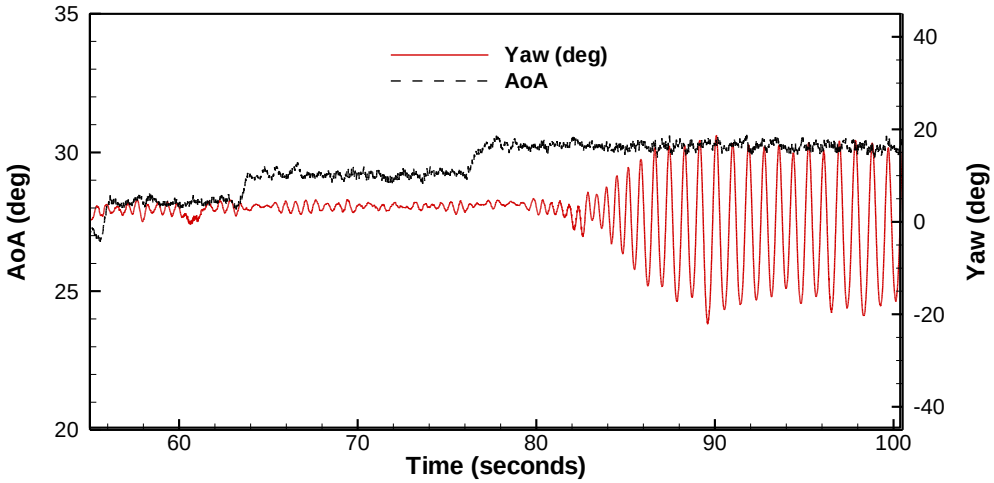

Figure 42: Time history of side slip expanded – yaw - free case

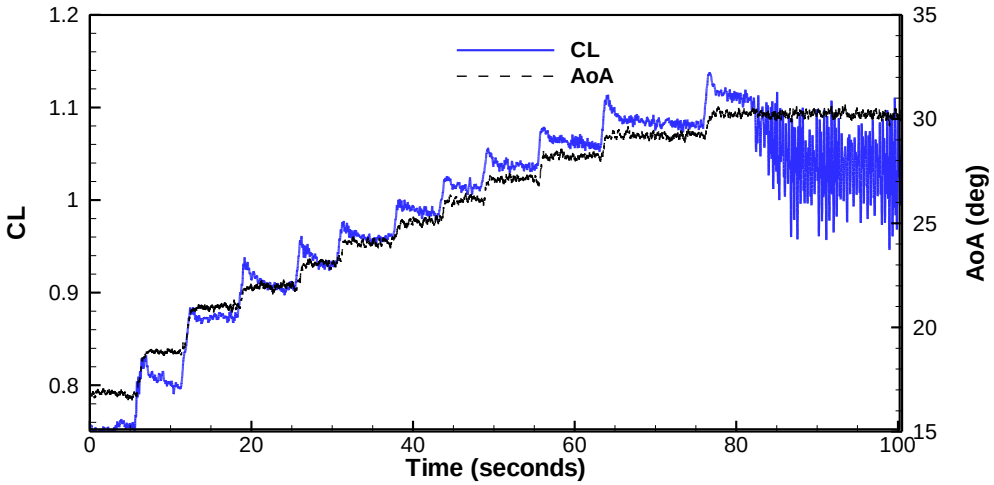

Figure 43: Time history of Lift expanded – yaw - free case

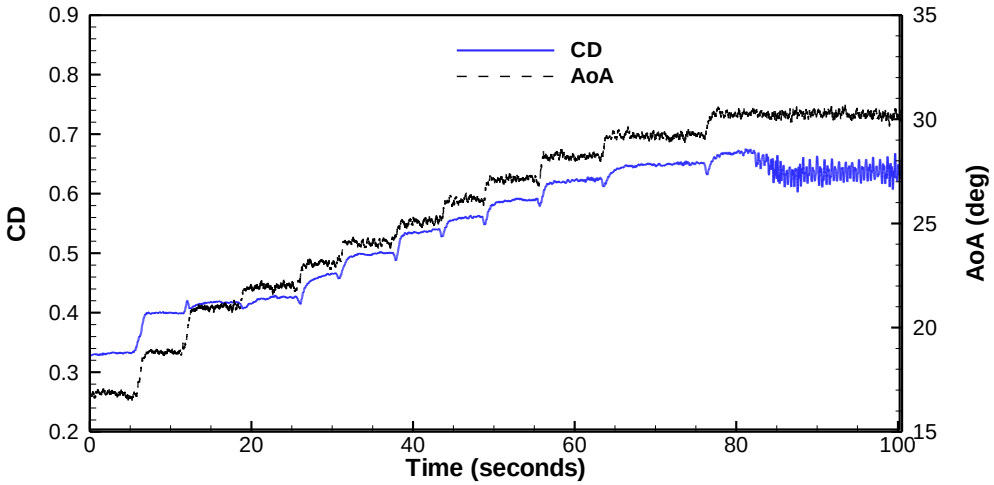

Figure 44: Time history of Drag - yaw - free case

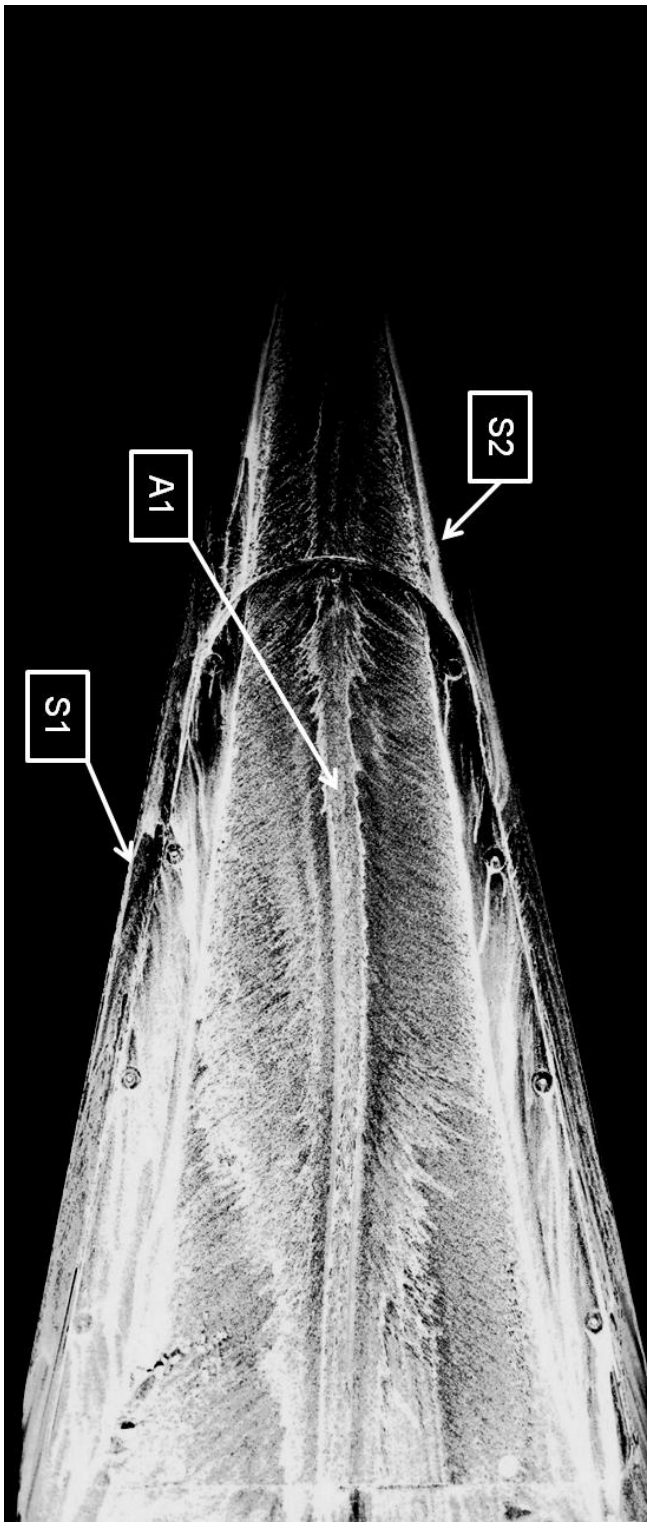

Figure 45: yaw - free case flow visualization

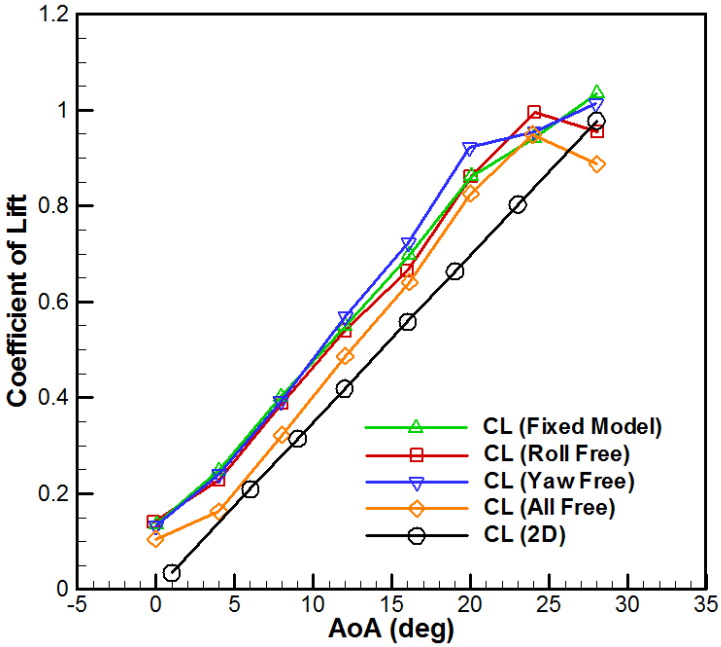

Figure 46: The Coefficient of Lift vs. AoA

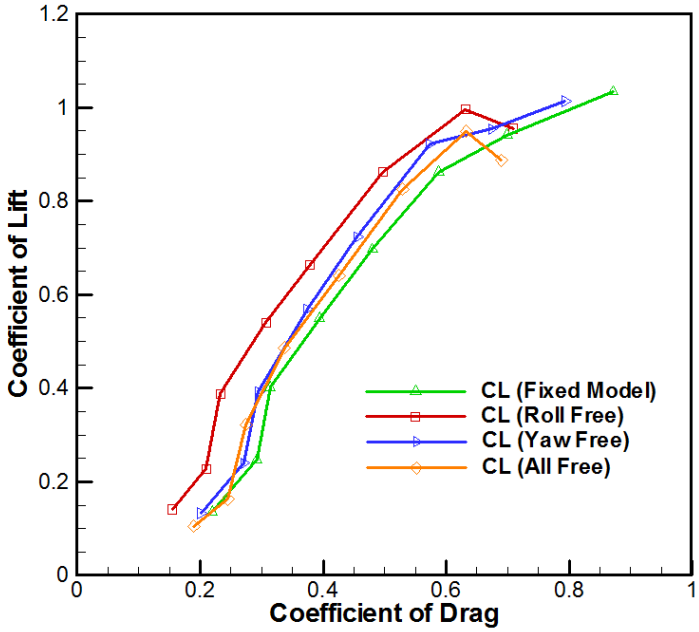

Figure 47: Drag Polar

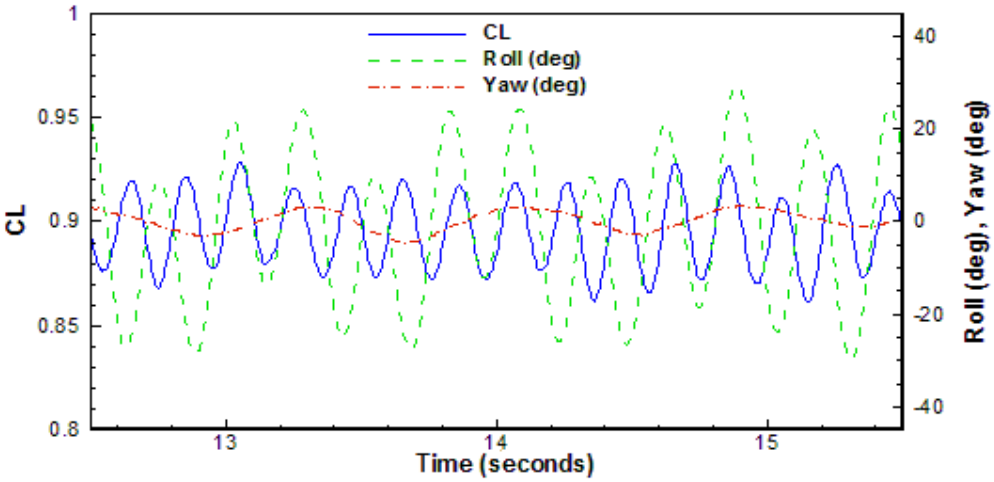

Figure 48: Time history of Lift, wing roll and side slip - all - free case

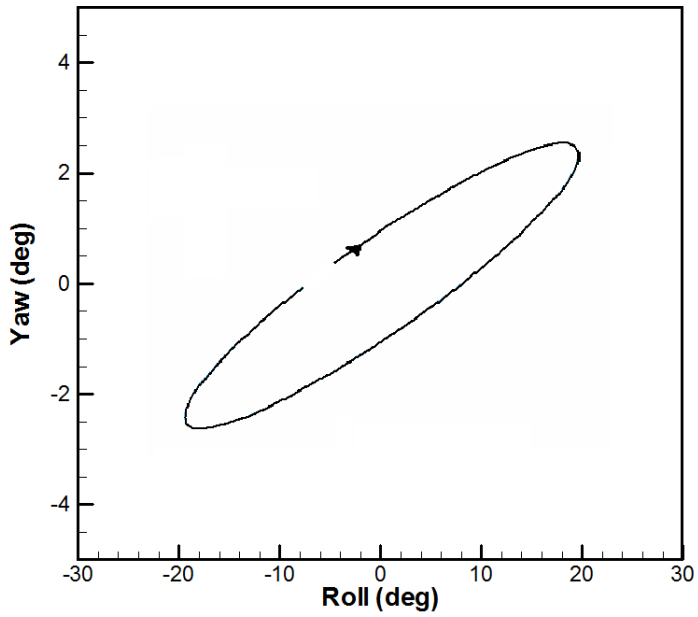

Figure 49: Yaw vs. Roll (All - free)

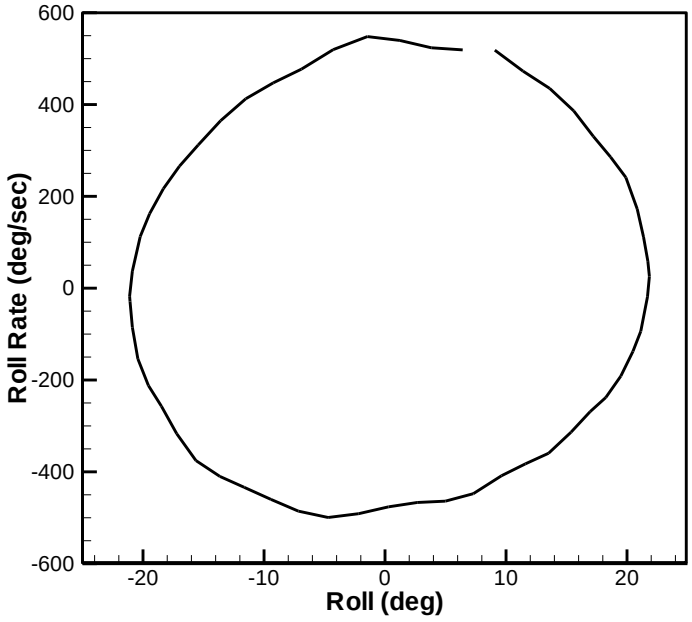

Figure 50: Phase Portrait of Roll – all - free case

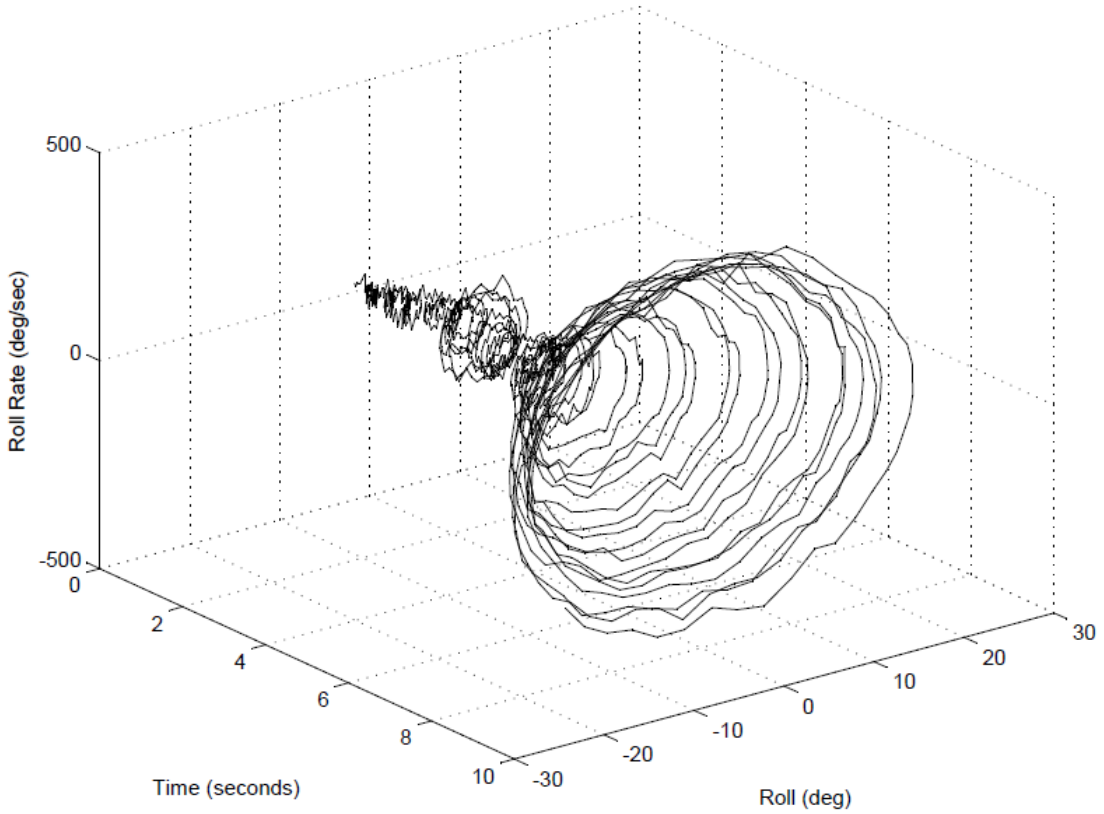

Figure 51: Extended Phase Portrait of Roll – all - free case

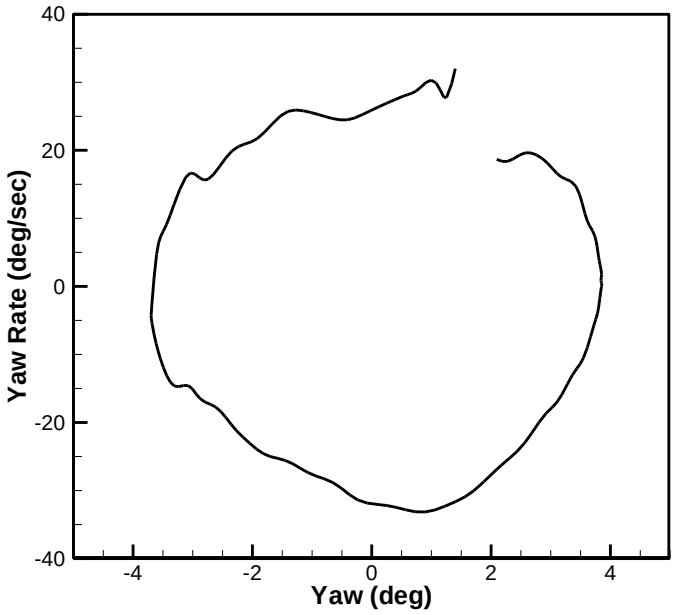

Figure 52: Phase Portrait of Yaw – all - free case

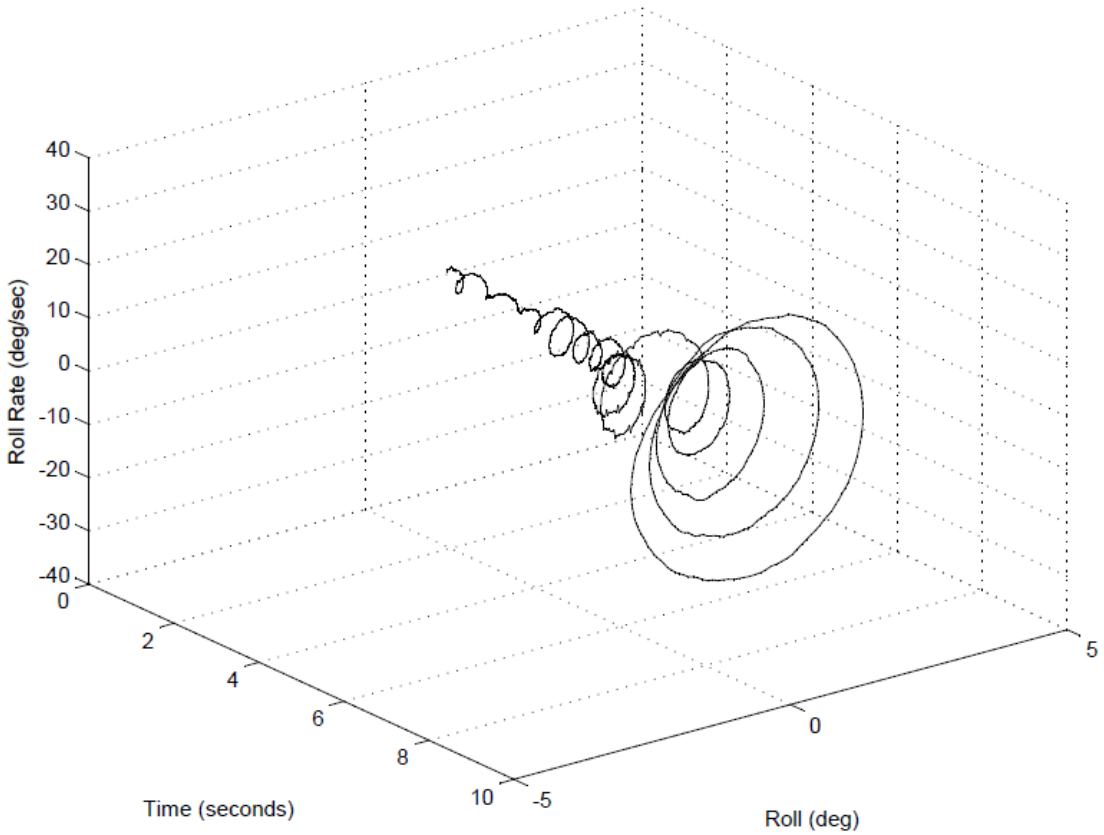

Figure 53: Extended Phase Portrait of Yaw – all - free case

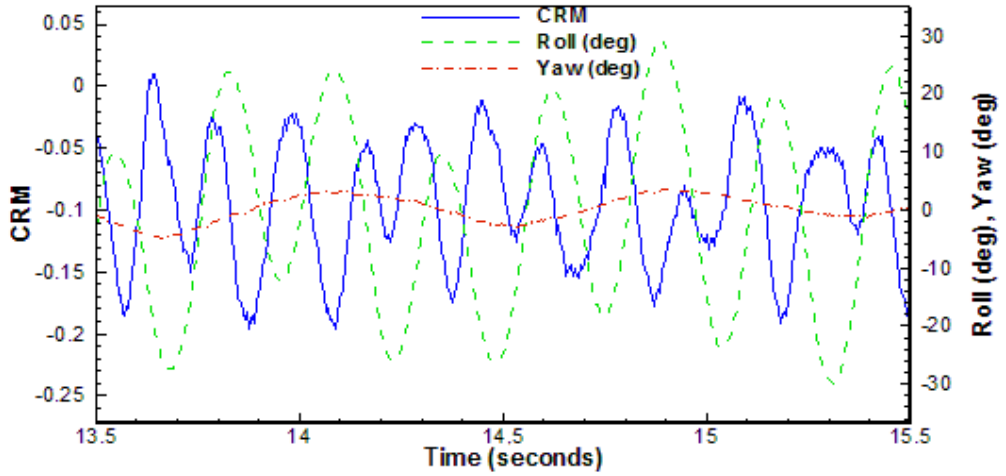

Figure 54: Time history of Rolling Moment, wing roll and side slip - all - free case

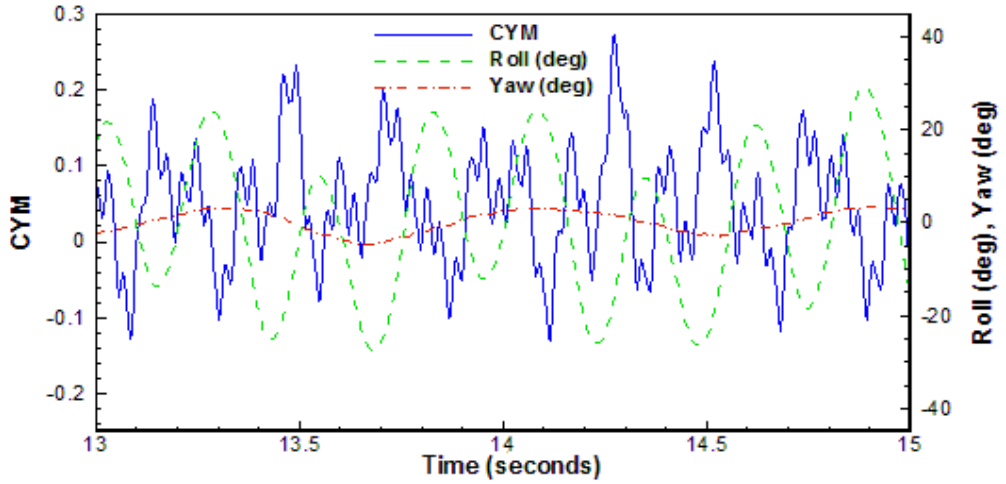

Figure 55: Time history of Yawing Moment, wing roll and side slip - all - free case

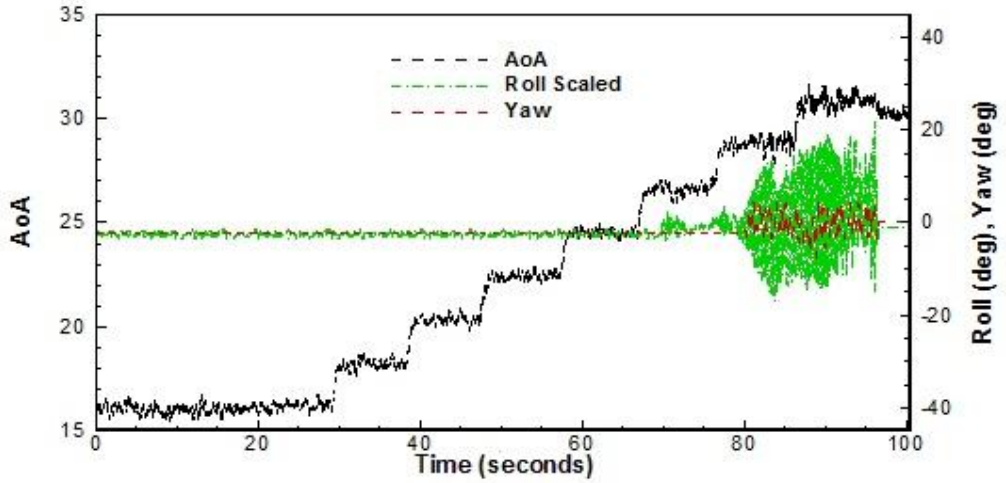

Figure 56: Time history of wing roll and side slip – all - free case

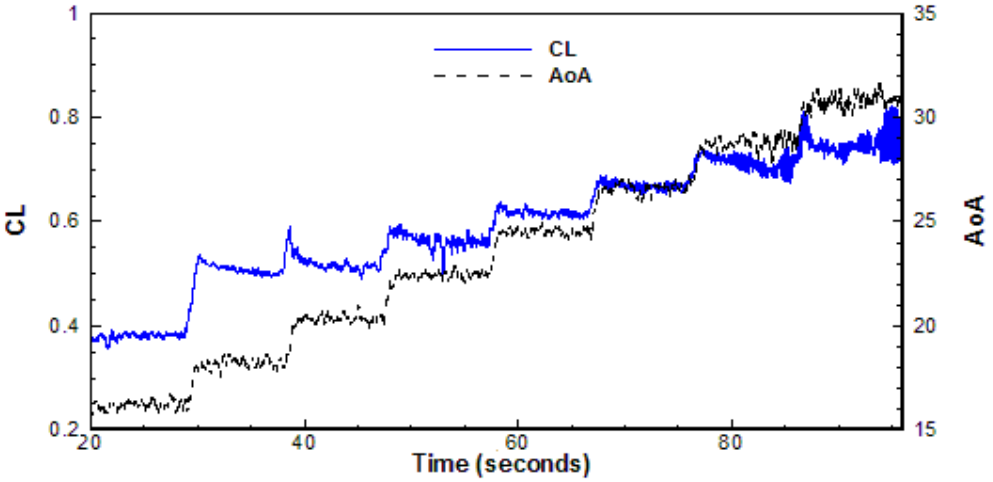

Figure 57: Time history of Lift - all - free case

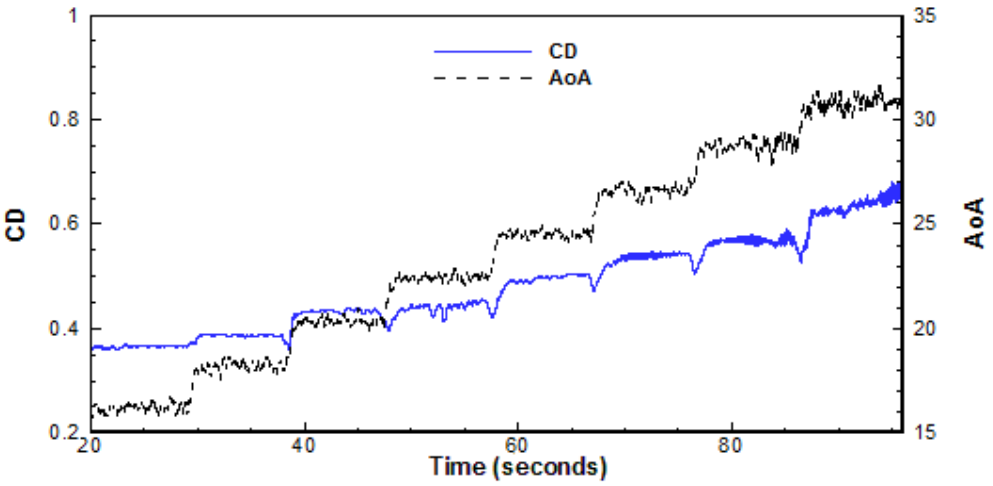

Figure 58: Time history of Drag - all - free case

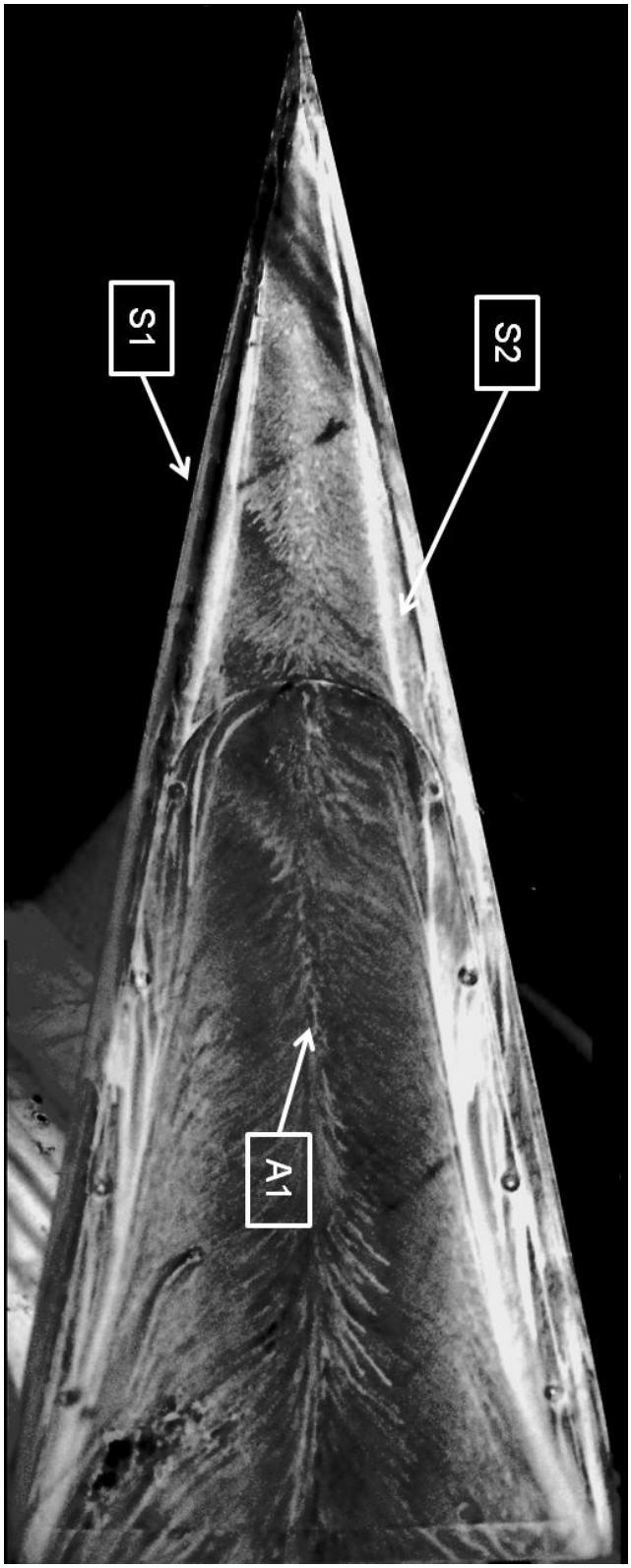

Figure 59: All - free case flow visualization

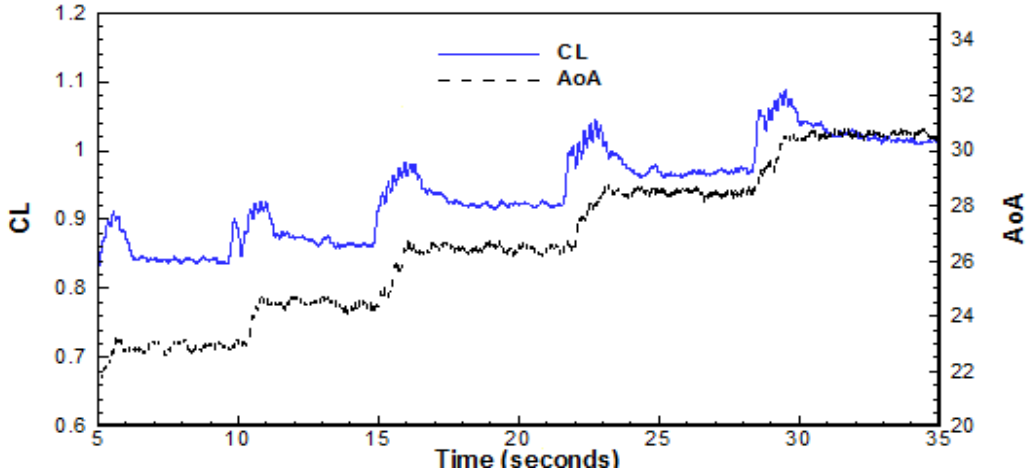

Figure 60: Time history of Lift – canard attachment

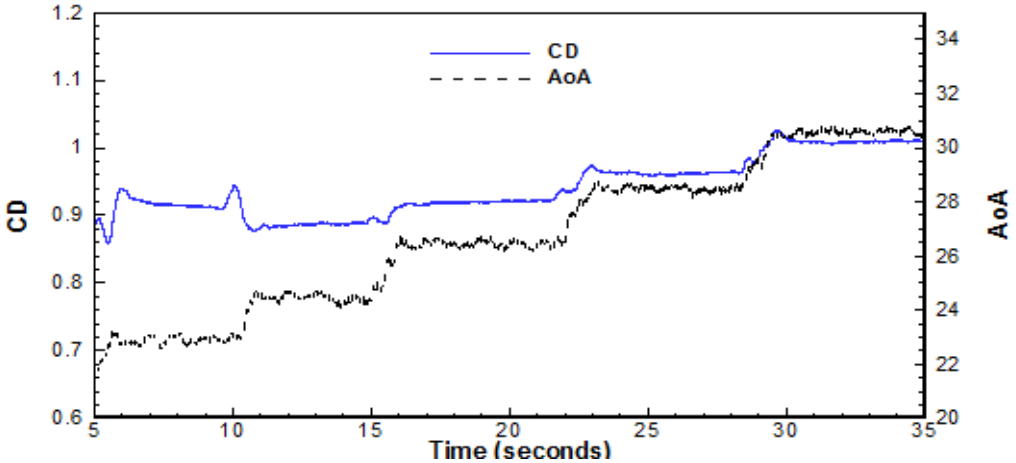

Figure 61: Time history of Drag – canard attachment

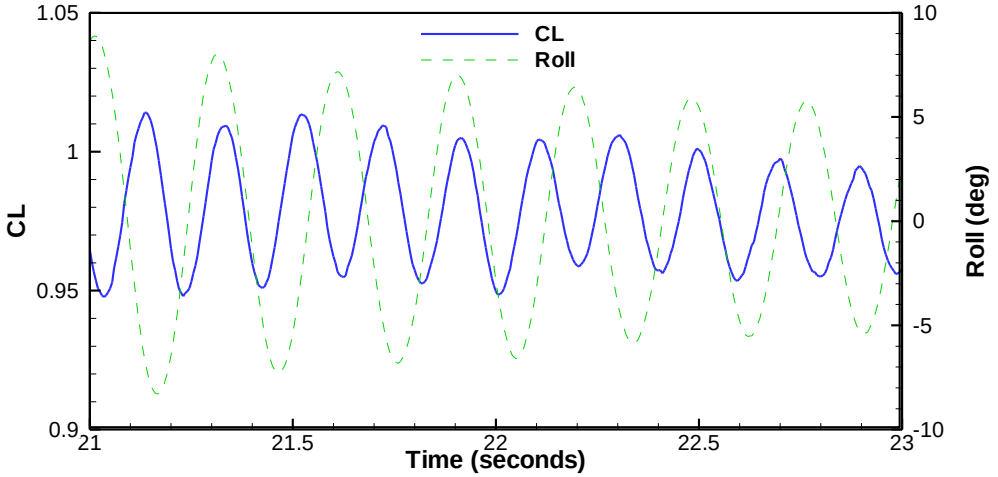

Figure 62: Time history of Lift and wing rock – canard attachment

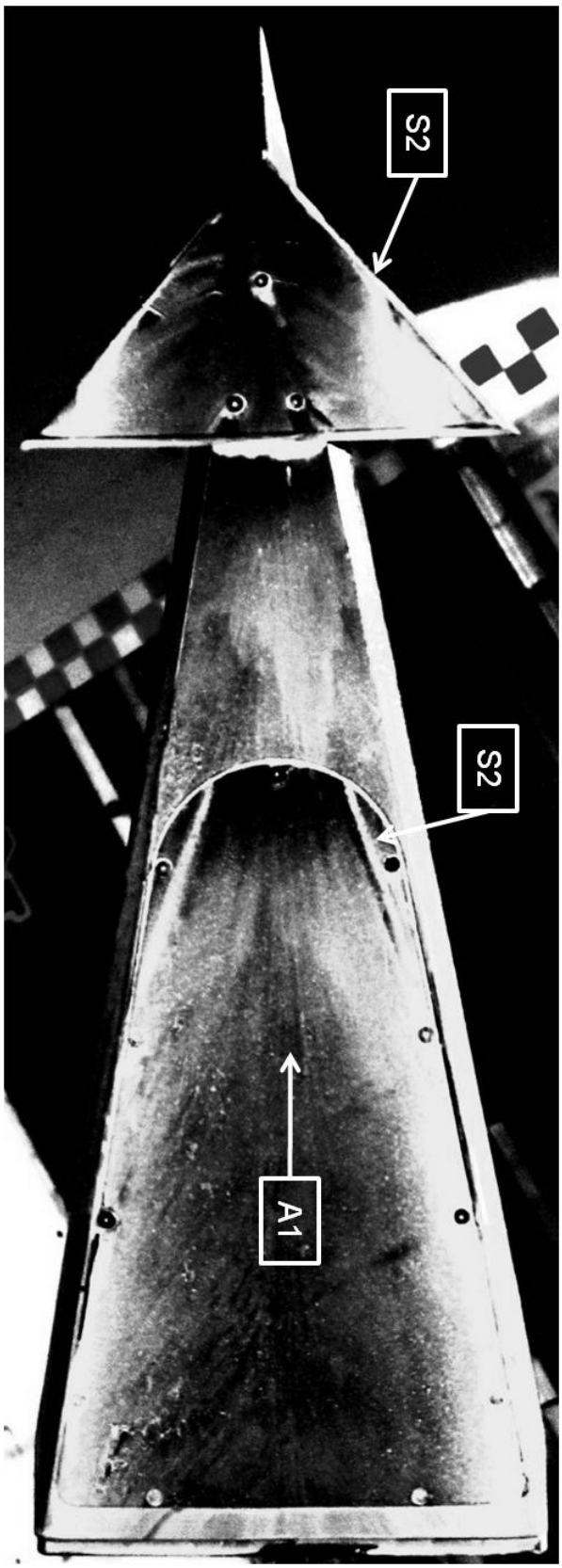

Figure 63: Canard attachment flow visualization

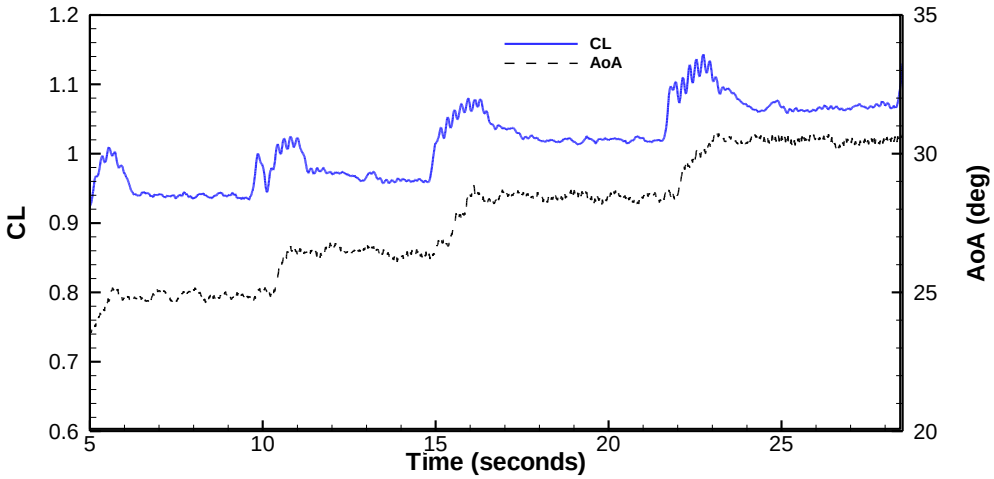

Figure 64: Time history of Lift – Double Delta attachment

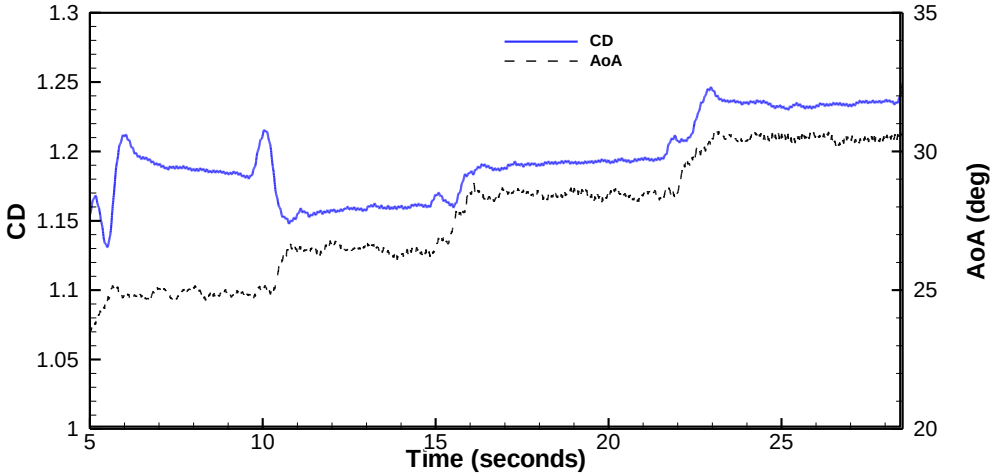

Figure 65: Time history of Drag – Double Delta attachment

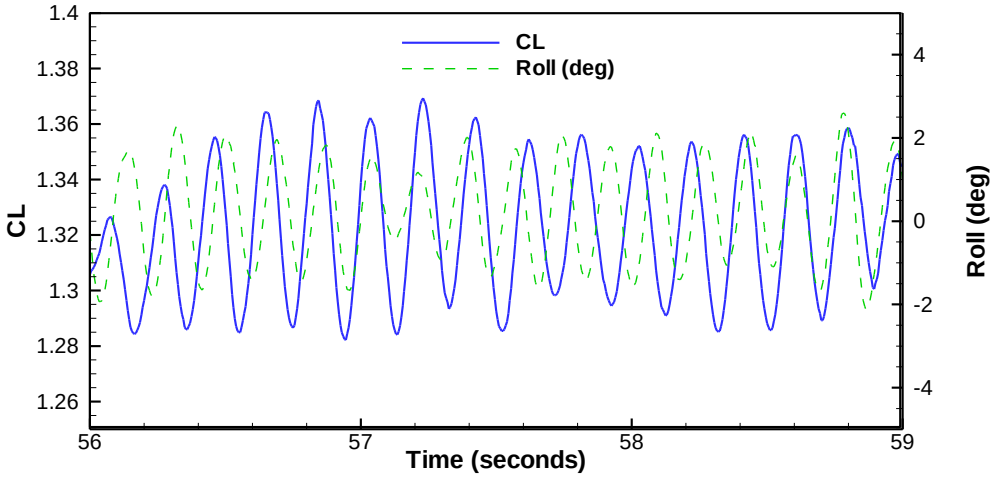

Figure 66: Time history of Lift and wing rock – Double Delta attachment

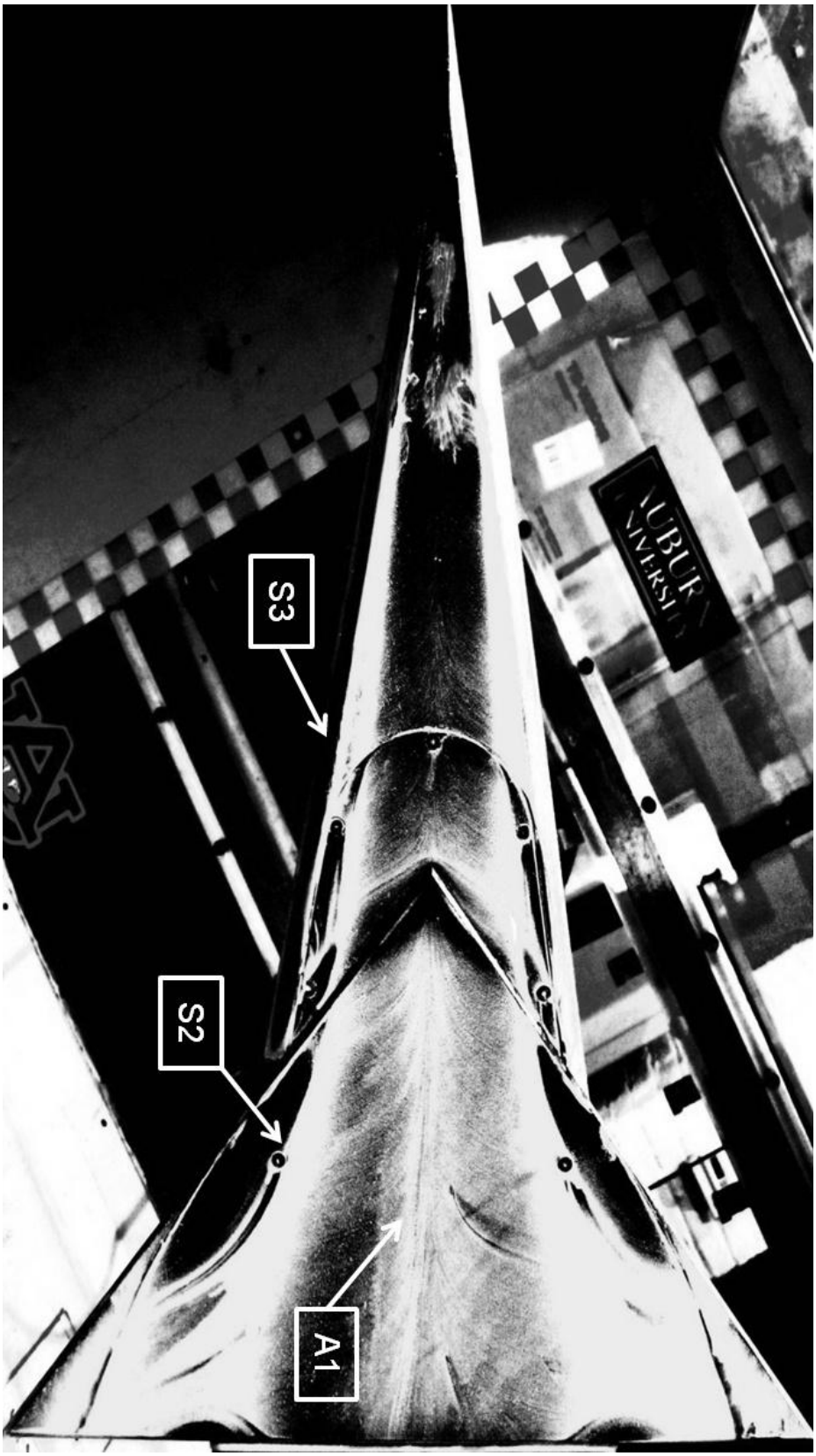

Figure 67: Double Delta attachment flow visualization

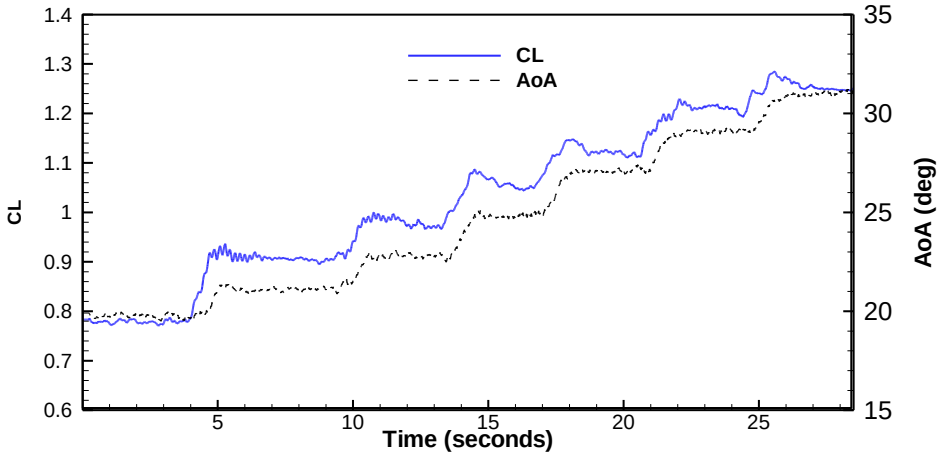

Figure 68: Time history of Lift – Canard and Double Delta attachment

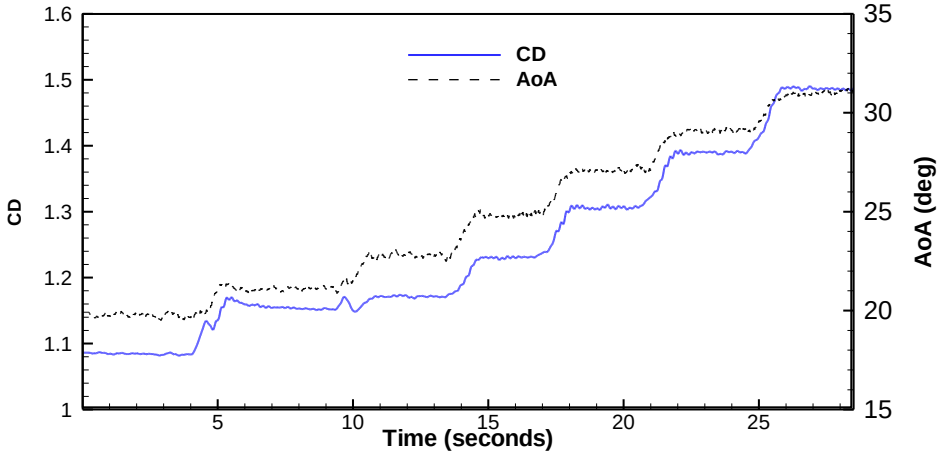

Figure 69: Time history of Drag – Canard and Double Delta attachment

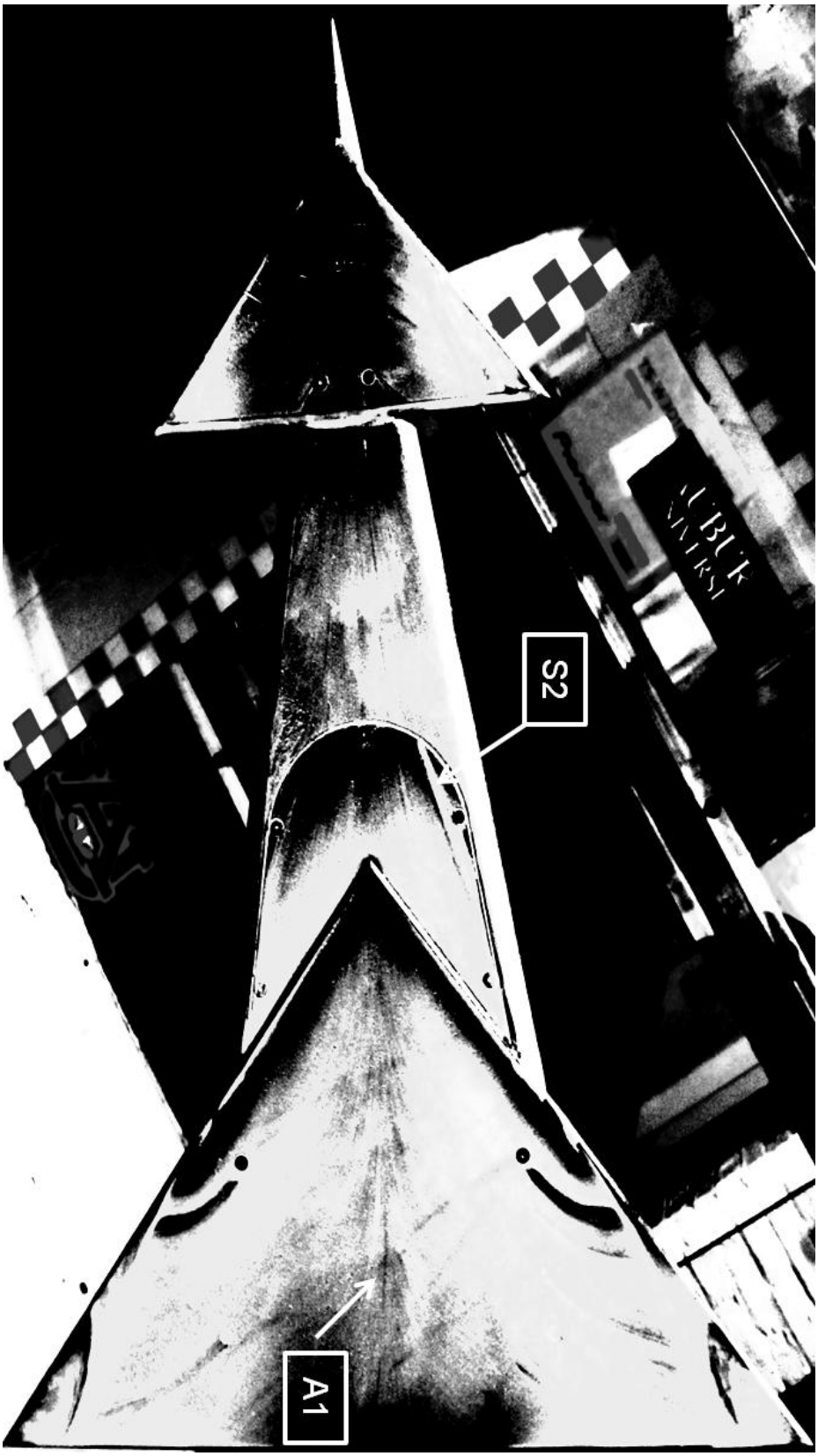

Figure 70: Canard and Double Delta Attachment flow visualization

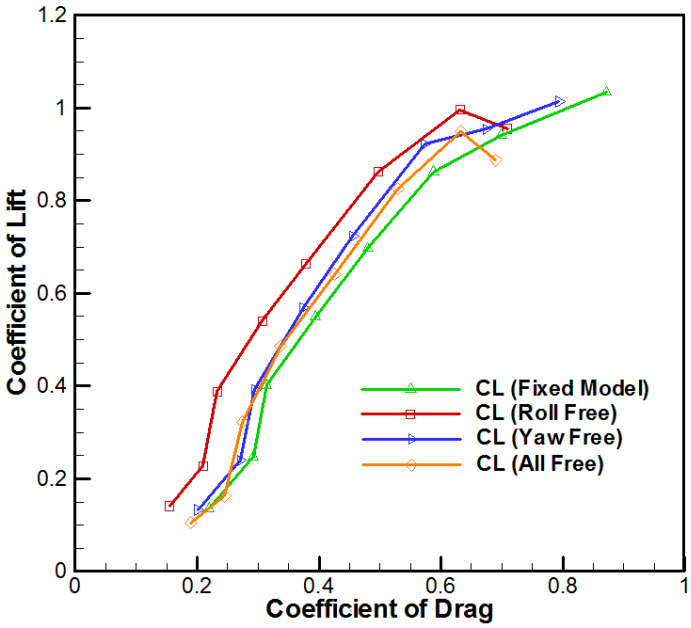

Figure 71: The Coefficient of Lift vs. AoA – passive flow control

Appendix B

List of Tables

Table 1: Reduction Matrix

Force or Moment	Normal	Pitching	Axial	Side	Rolling	Yawing
Normal	17.7596	0.5705	0.2023	0.0082	-0.0734	0.1968
Pitching	0.0738	-4.140	0.001	0.0589	-0.0216	0.0095
Axial	0.0499	-0.2768	3.7944	-0.2085	0.037	0.1518
Side	-0.2857	-0.066	0.0193	10.3528	0.6452	-0.0425
Rolling	0.0164	0.0312	-0.0137	0.0067	4.4716	-0.017
Yawing	0.0227	-0.0339	-0.0051	0.2168	-0.0154	-7.0653

Table 2: Optical Encoder Parameters [48]

Parameter	Dimension
Shaft Speed	6,000 RPM max. continuous
Acceleration	1x10^5 rad/sec²
Starting Torque	.70 oz-in typical
Shaft Loading	5 lbs. max.
Weight	11.5 oz.
Shaft Runout	.030" axial .010" TIR
Shaft Insertion Depth	1.4" max. with default cover. No limit with H-option cover.
Moment of Inertia	3.7x10^-3 oz-in-sec²
Vibration	20 g. 5 to 2KHz
Shock	50 g. @ 11mS

Table 3: Honeywell HC1512 sensor parameters [49]

Supply	Vbridge (Vb) referenced to GND	1.0	5.0	25	Volts
Resistance	Bridge current = 1mA	2000	2100	2800	ohms
Angle range	>Saturation Field	-90		+90	deg
Sensitivity	Vb=5 volts, field=80Oe				
	@ zero crossing		2.1		mV/°
	@ zero crossing averaged in a 45° range		1.8		mV/°
Output Voltage	Vb=5 volts, field=80 Oe	100	120	140	mVpp
Bridge Offset	field=80 Oe				
	Bridge A	-7	0	+7	mV/V
	Bridge B	-7	0	+7	mV/V
Resolution	BW=10Hz, Vb=5 volts		0.05		deg
Noise Density	@1Hz, Vb=5 volts		70		nV/sqrt Hz

Appendix C

Additional Plots

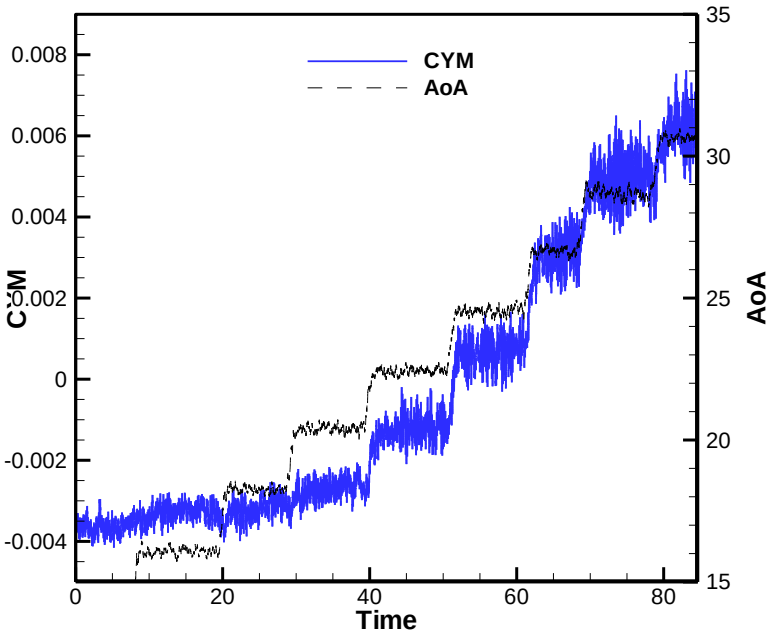

Figure 72: C_{YM} and AoA vs. Time - fixed wing

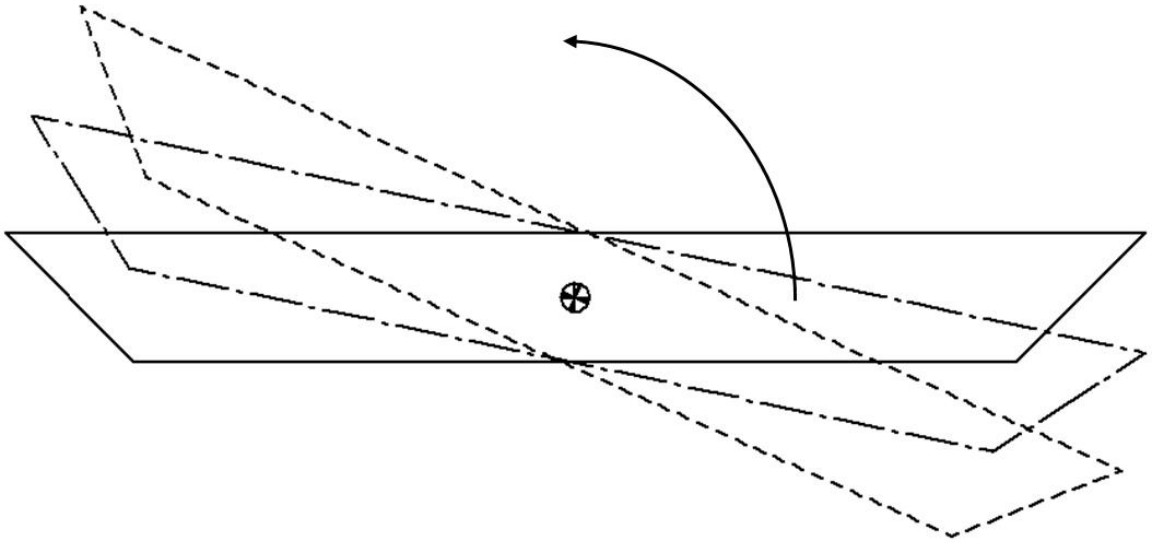

Figure 73: Roll Coordinate System

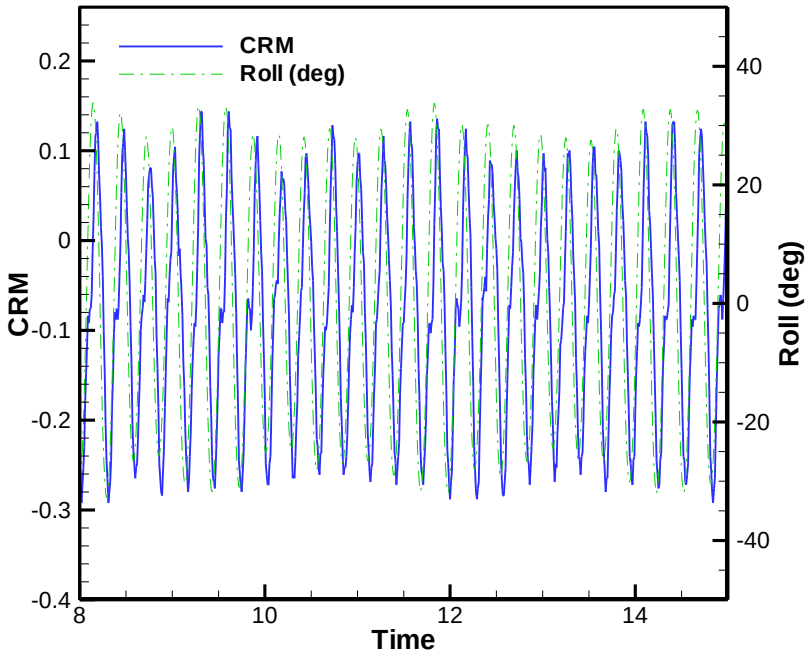

Figure 74: Roll and C_{RM} vs. Time (b) – Roll - free

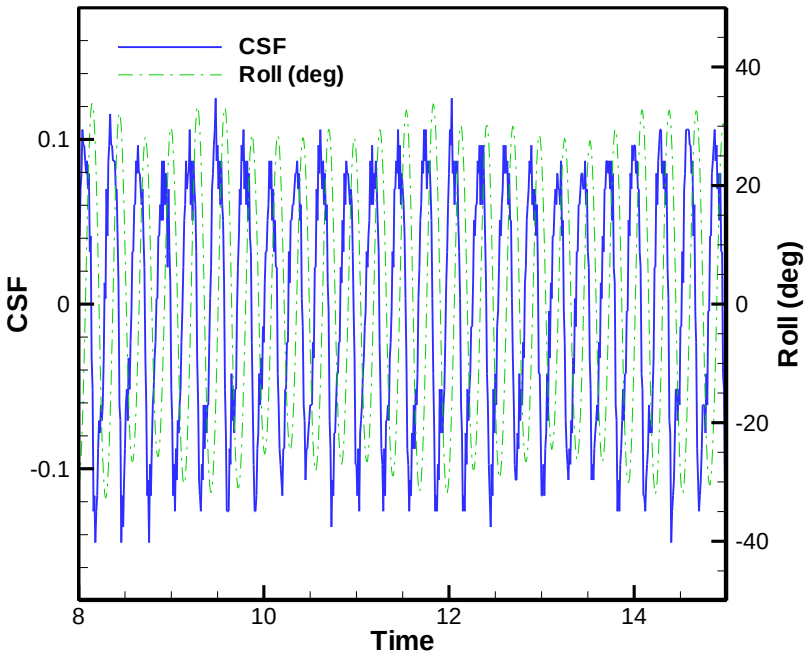

Figure 75: Roll and C_{SF} vs. Time (b) - roll - free

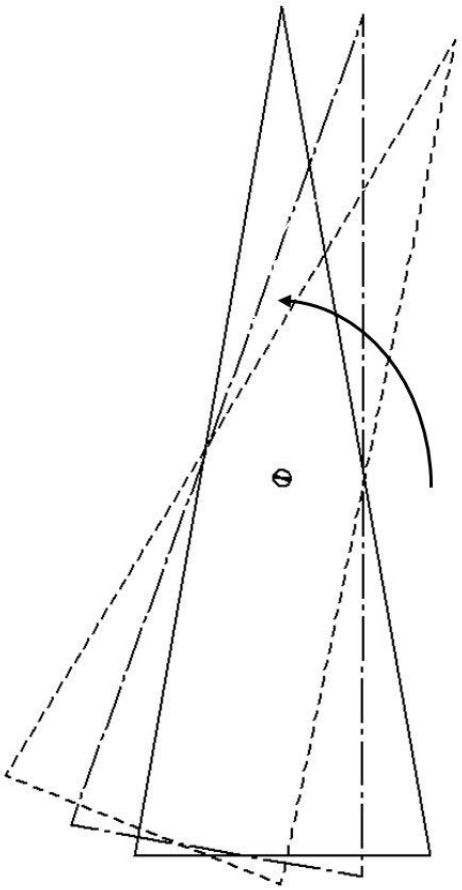

Figure 76: Yaw Coordinate System

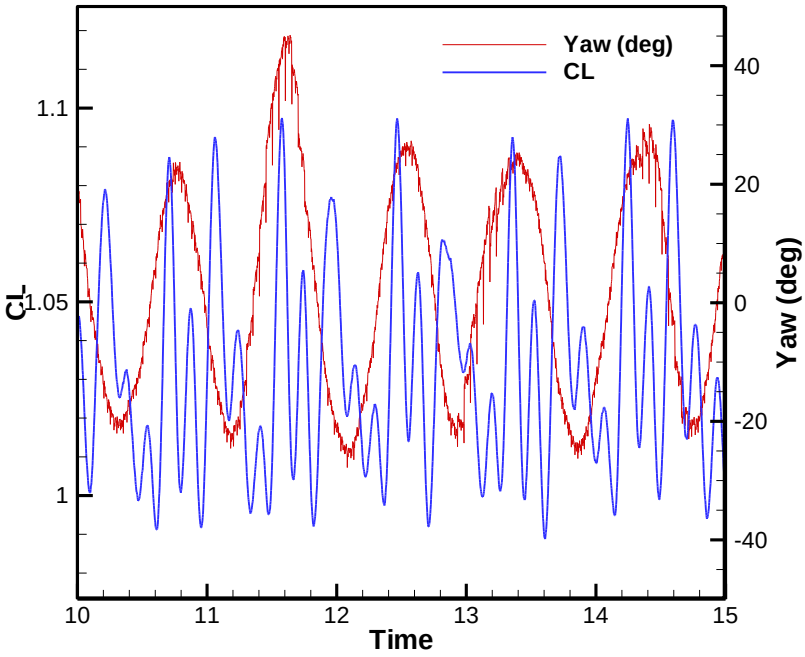

Figure 77: Yaw and C_L vs. Time (b) - yaw - free

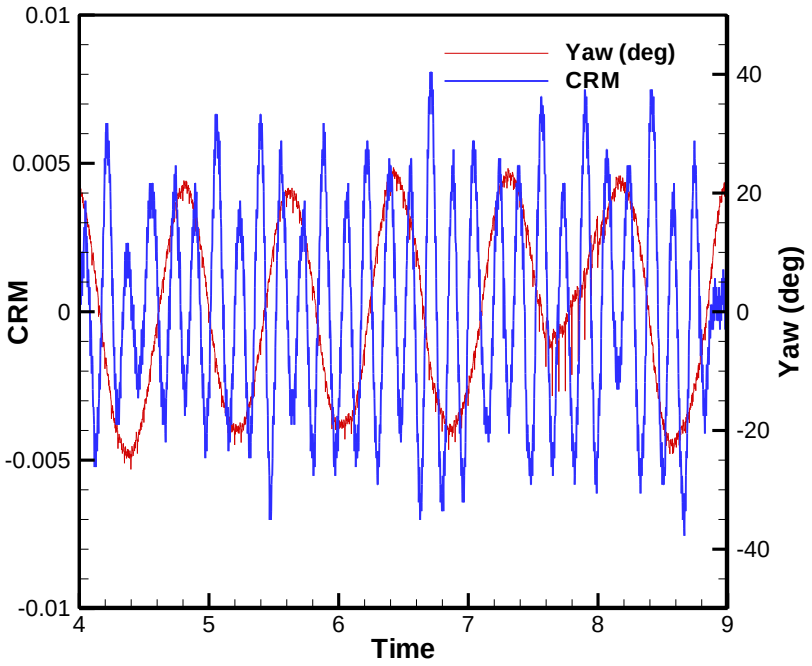

Figure 78: Yaw and C_{RM} vs. Time (b) - yaw - free

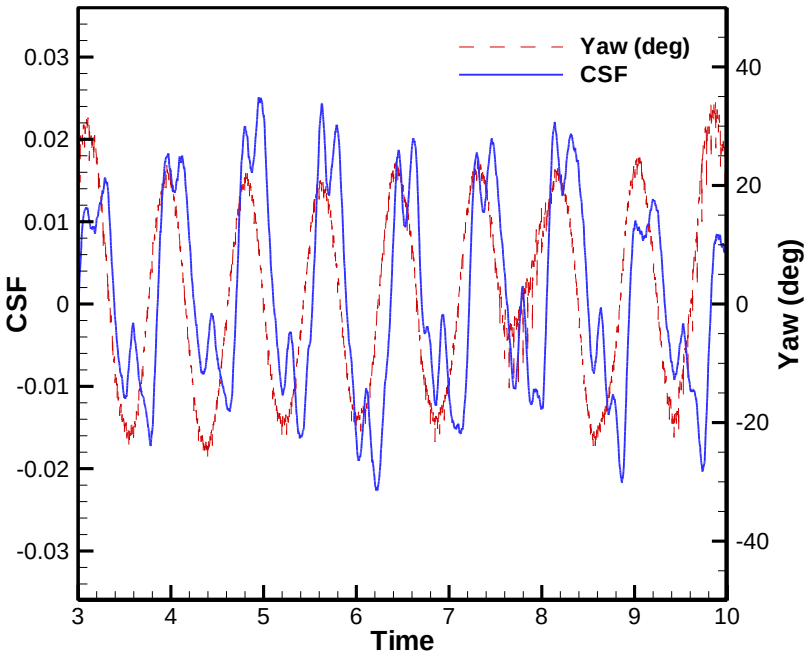

Figure 79: Yaw and C_{SF} vs. Time (b) – yaw - free

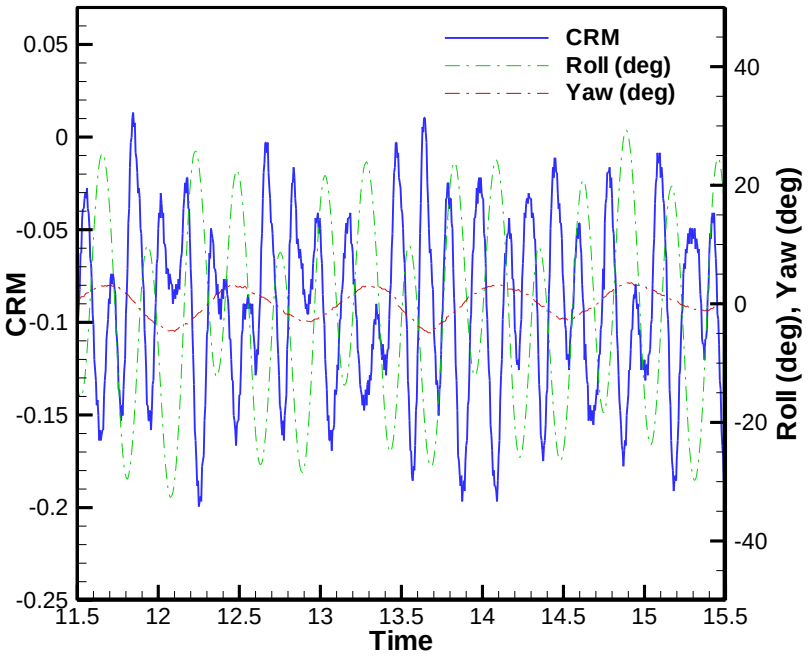

Figure 80: Roll, Yaw and C_{RM} vs. Time (b) - all - free

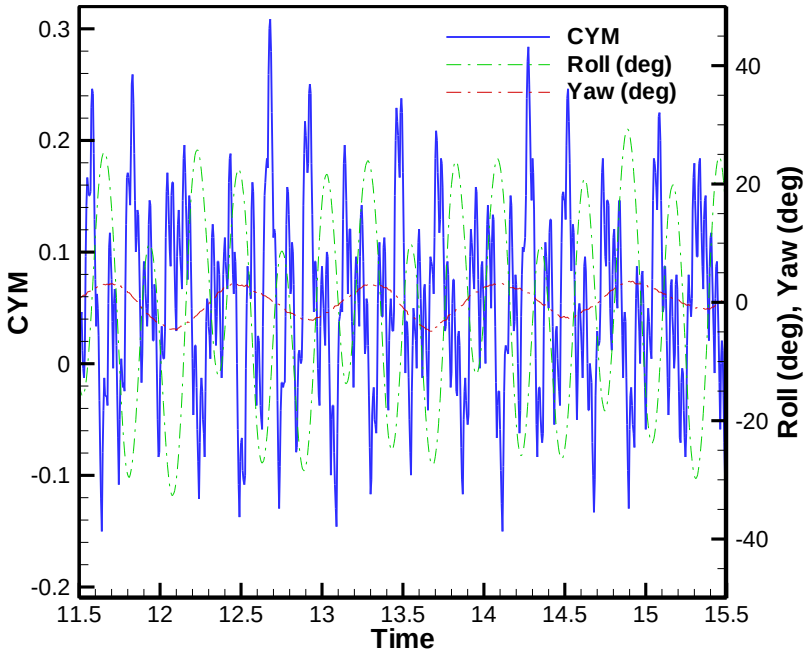

Figure 81: Roll, Yaw and C_{YM} vs. Time (b) - all - free

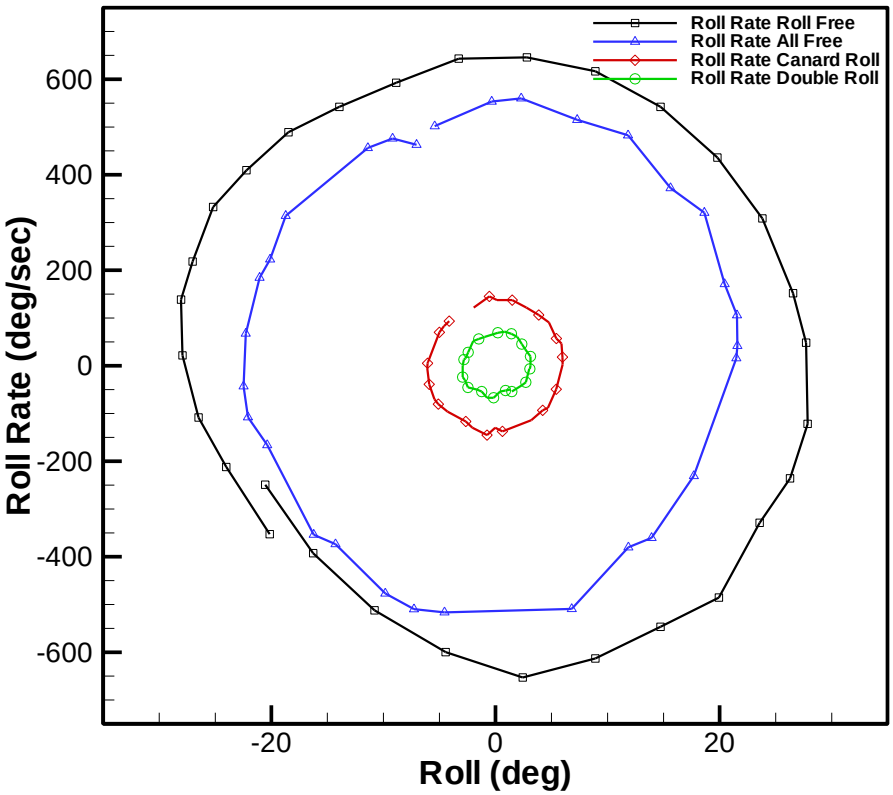

Figure 82: All Cases Phase Portraits

Appendix D

Uncertainty Analysis

An uncertainty analysis was performed to ensure confidence in the data obtained during experimentation. The standard deviation was obtained for each oscillation dataset to conduct this analysis. The average of the standard deviation for the roll - free case oscillation was 2.73 % for maximum roll and 1.13 % for minimum roll. The average of the standard deviation for the yaw - free case oscillation was 3.26 % for maximum yaw and 2.47 % for minimum yaw. This uncertainty value was assumed to be negligible and therefore the measured data was concluded to be precise.